

From Spheres to Cones: Structural Instabilities and Acidity at Conical Regions in Trivalent Metal Ion Nano-clusters

Jihong Shi, Han Nguyen, Mateo Pescador Arboleda, and Styliani Consta*

*Department of Chemistry, The University of Western Ontario, London, Ontario, Canada
N6A 5B7*

E-mail: sconstas@uwo.ca

Abstract

Sub-nanometer aqueous clusters containing a single trivalent metal cation can exhibit charge-induced structural instabilities. Here, we present computational evidence that clusters containing a single Fe^{3+} , Lu^{3+} , or La^{3+} ion undergo continuous geometric transformations as a consequence of this instability. These clusters dynamically evolve across their potential energy landscape, adopting triangular, elongated two-point, single-point, and more spherical configurations often with distinct conical surface protrusions. The manifestation of this instability differs from that observed in mesoscopic and microscopic droplets containing macroions, where stable “star-like” structures form, characterized by a specific number of conical protrusions that varies with the droplet size. In the present study, we find that the orientation of the H_2O molecules surrounding the metal ion is influenced not only by the electric field of the trivalent ion but also by the local conical protrusions. To further investigate the local acidity in the conical protrusions, we employ a proxy model system consisting of an aqueous nano-cluster containing three H_3O^+ ions, simulated using ab initio molecular dynamics. Within the conical regions of the cluster, protons exhibit diffusion across several water molecules, in contrast to the more localized proton delocalization observed in the compact body of the cluster. These findings suggest that local geome-

try can significantly modulate acidity in highly charged nano-clusters, with potential implications for understanding charge-transfer and ionization mechanisms in techniques such as electrospray ionization mass spectrometry. Additionally, the structural motifs and solvent organization reported here provide a molecular-level framework that can complement interpretations from infrared spectroscopic data.

Introduction

Universality in the manifestation of physico-chemical properties across system sizes—from sub-nanometer clusters to microscopic droplets—is unusual. For instance, phenomena such as melting and freezing,^{1,2} chemical reactivity,^{3,4} and ion solvation exhibit a strong dependence on system size.^{5,6} In this work, we investigate charge-induced instability in clusters containing a single trivalent metal ion, exploring how this instability varies with both ion type and cluster size, and examining its implications for infrared spectral features.

A fundamental model due to Lord Rayleigh predicts the conditions of stability of a charged fluctuating droplet arising from its energy, which is expressed as the sum of the electrostatic energy and surface energy.^{7–9} A linear stability analysis of the model leads to the Rayleigh limit.^{7,8} Mathematically, the Rayleigh limit of a conducting droplet is defined via the

dimensionless Rayleigh fissility parameter, X , expressed as

$$X = \frac{Q^2}{64\pi^2\gamma\epsilon_0 R^3} \quad (1)$$

where Q is the droplet charge, γ the surface tension, ϵ_0 and R are the permittivity of vacuum and the radius of the droplet, respectively. When $X = 1$ (Eq. 1) in a conducting droplet the droplet is at the Rayleigh limit. A droplet's Rayleigh limit is defined at the point where the surface tension forces that tend to compact a droplet are counterbalanced by the repulsive Coulomb forces among the unbalanced charges of the same sign.

A distinction between the stability of a conducting droplet⁷⁻⁹ and of a droplet containing a single ion in a dielectric medium⁹ is discussed now. In a conducting droplet, the charge carriers are many separate ions and the Rayleigh limit is given by $X = 1$ in Eq. 1. When the stability of a droplet containing a single ion, such as a lanthanide series trivalent ion or an ionized nucleic acid, in a dielectric medium is studied then X is determined by Eq. 7 in Ref. ⁹ For a certain value of the dielectric constant of the droplet, Eq. 7 yields the minimum value of X by varying the order, l of the spherical harmonics (it is noted that spherical harmonics are used to expand the droplet's shape fluctuations). Then the value of X is used in Eq. 1 to estimate R . Another related difference between a conducting droplet and a single ion in a fluctuating spherical dielectric medium is that in the former case the first mode to become unstable is the $l = 2$, while in the latter case the mode depends on the dielectric constant of the droplet.⁹ It is noted that the Rayleigh limit of a conducting droplet arises from the generalized Rayleigh model for a dielectric droplet presented in Ref. ⁹ when the droplet's dielectric constant tends to infinity. In a conducting droplet, the instability manifests as Rayleigh jets that emit a train of charged sub-droplets^{10,11} from a larger parent droplet, while in a dielectric droplet in the form of "star-like"-shaped droplets.¹²

Computational evidence has shown^{9,12,13} that mesoscopic and microscopic droplets charged

with a single macroion (e.g. a DNA molecule or an ionized protein) obey the predictions of a generalized Rayleigh's continuum model^{7,8} for the onset of the charge-induced instability. Computations have also shown that at the instability regime the spherical shapes transform into stable "star-like" morphologies,^{9,12-14} where the number of points in the stars increases sequentially from one at the onset of instability to several for system parameters deeper into the instability regime.

The generalized Rayleigh's model⁹ is based on a linear stability analysis for small fluctuations of the spherical shape. Sub-nanometer sized clusters differ from the larger droplets in that their physical chemistry is entirely dominated by the free surface and the large relative shape fluctuations. Therefore, it is hypothesized that in sub-nanometer sized clusters the Rayleigh model predictions for the onset of instability and the stable shapes in the instability regime may differ from those in larger droplets.

In our study, the examples of Fe^{3+} , Lu^{3+} , La^{3+} in aqueous clusters of sizes containing a few tens to a few hundreds of H_2O molecules are examined. Trivalent ions are selected because it is expected that the manifestation of the instability will be more pronounced in these higher charged ions than in the monovalent and divalent ions. The specific ions are selected as paradigms to demonstrate the dependence of the phenomena on the ion size.

Recognizing the instability regime in clusters comprised a few tens to a few hundreds of H_2O molecules and a trivalent metal ion is of practical importance for a number of experiments that measure the infra-red (IR) spectra of H_2O molecules in these cluster sizes.^{15,16} Experimental methods such as black body infrared radiative dissociation (BIRD), and ensemble infrared photodissociation (IRPD) may probe the extent at which an ion's electric field influences the structure of the surrounding hydration shells.¹⁷ These methods can be applied to clusters comprised a single ion and a few tens of H_2O molecules up to several hundreds H_2O molecules.¹⁵ Williams et al. demonstrated that the IR spectra of aqueous clusters comprised a single monovalent, divalent and trivalent ion

in 36 H₂O molecules, reflect the reorganization of the hydrogen-bond network induced by the ion’s electric field, with a red shift in the free-OH (found in the cluster surface) stretching band proportional to the ion’s charge.¹⁵ The ion-induced patterning in the aqueous clusters provided evidence that the effect of multivalent ions beyond the first hydration shell in the bulk solution is considerable. This is in agreement with the simulation results presented here that show that indeed the electric field of the trivalent ion, regardless of its size, strongly influences its immediate two hydration shells. We further show that the effect of the collective electric field from the ion and the other H₂O molecules in the third and farther hydration shells orients the H₂O molecules differently in clusters subject to instability relative to clusters outside the instability regime. The difference implies that the ion’s electric field also influences the third and partially fourth hydration shell in clusters that are subject to instability. As it will be shown, in clusters where the effect of the instability has ceased, the trivalent ion is located by approximately three hydration shells below the surface. The orientation of the third hydration shell, which also includes surface H₂O molecules, is influenced differently by Fe³⁺, Lu³⁺, La³⁺, depending on the ion’s size.

The charge-induced instability shapes are characterized by conical protrusions on the cluster surface. For the first time, the acidity of the H₂O molecules in the conical protrusions, and consequently, their ability for proton transfer, is examined here. To probe the chemical reactivity in these highly convex regions, we use a proxy simulation set-up, where an aqueous cluster charged with three H₃O⁺ ions is modeled by ab initio molecular dynamics (AIMD). It is found that in a conical protrusion that persists for a few picoseconds of AIMD simulation, there is rapid proton diffusion over several H₂O molecules, unlike proton delocalization over two or three H₂O molecules found in the compact body of the cluster. The proton diffusion in the extruded regions complements studies that have been performed on the proton transfer in bulk solution along H₂O chains.^{18–31}

Understanding trivalent metal ion-H₂O inter-

actions is significant on its own merits. These interactions play an important role in solution chemistry as for example in liquid-liquid phase separation (LLPS) of proteins.³² Nevertheless their role in LLPS is less studied than the water-alkali and alkaline earth ions. Specific ordering of H₂O molecules or of other solvents induced by a multi-valent ion in clusters may be also important in catalysis. Metal ion-solvent clusters comprised up to approximately twenty solvent molecules have been actively explored over several decades for their distinct hydration and catalytic properties.^{4,17,33–39}

Preparing clusters of trivalent metal ions of the desired size in IR experiments poses a challenge because the metal ion may undergo hydrolysis within the cluster or the metal ion is electrosprayed already hydrolyzed from the parent bulk solution. Williams et al. have reported^{15,40} that the experimental conditions under which the metal ions in the lanthanide series do not hydrolyze in nanodroplets have been found, while Fe³⁺ always been detected in its hydrolyzed form possibly because it is already hydrolyzed in the parent bulk solution. In the present study the molecular modeling of Fe³⁺-H₂O clusters does not allow for the hydrolysis reaction but it assists along with Lu³⁺ and La³⁺ to establish a trend that shows the dependence of the phenomena on the ion size.

In our study the majority of the simulations are performed at the lowest possible temperature, 190 K, where the H₂O molecules are still mobile and the energy transfer to the rotational motion of the cluster does not freeze the internal motions of the molecules. However, the experiments are performed at cryogenic temperatures (\lesssim 133 K), where the metal ion clusters are likely to be in ice-like states.⁴¹ The manifestation of the instability at a temperature where the H₂O dynamics is very slow is also presented in this study. However, the emergence of ice-like structures as a function of cluster size when the dynamics is very slow deserves its own study that we currently perform.

Methodology

Here we present the main points of the computational methods. A detailed account of the methodology is found in Sec. S1-S3 in SI. Systematic studies of molecular dynamics (MD) of aqueous clusters charged with a single Fe^{3+} , Lu^{3+} , or La^{3+} ion were performed using the Nanoscale Molecular Dynamics⁴² (NAMD) v 2.14 software and visualized by Visual Molecular Dynamics⁴³ (VMD) v 1.9.4. The clusters were comprised of $N_{\text{H}_2\text{O}} = 32 - 242$ and a single Fe^{3+} , Lu^{3+} , or La^{3+} ion. A few simulations were also performed with $N_{\text{H}_2\text{O}} = 800$ and a single Fe^{3+} , Lu^{3+} , or La^{3+} ion. MD simulations were also performed for pristine aqueous clusters with $N_{\text{H}_2\text{O}} = 70$ and 242 for using them as reference systems. The water molecules were modelled by the TIP3P-CHARMM model⁴⁴ and the ions by the parameters reported in Ref.⁴⁵ We note here that the parameters for Fe^{3+} from Ref.⁴⁵ lead to a first hydration shell with ~ 4 H_2O molecules surrounding the ion. This is to be contrasted with the coordination number of six that is found in experiments. Regardless of the low coordination number of Fe^{3+} , the Fe^{3+} model still shows that the phenomena observed here do not depend on fine details of the force field. For Lu^{3+} , or La^{3+} the coordination number in the first hydration shell is in agreement with the experiments. The systems were simulated at temperature $T = 90$ K, 130 K, 190 K and 250 K. Among the tested temperatures, $T = 190$ K was selected to perform the majority of the simulations because at this temperature the molecules in the clusters are still diffusing within the simulation time. At $T = 90$ K and 130 K the clusters demonstrate deformations caused by the instability but there is no internal motion of the H_2O molecules and the ion within the simulation time.

To study the proton diffusion a cluster containing 64 H_2O molecules and $3\text{H}_3\text{O}^+$ ions were also simulated using *ab initio* Born-Oppenheimer MD (BOMD) in CP2K v 9.1 software package.⁴⁶ The validation of the simulation protocol is presented in Sec. S4 in SI. The system was simulated at $T = 300$ K using a Nosé-Hoover thermostat. The protonated clus-

ter was placed in a large vacuum box of dimensions $48 \times 48 \times 48 \text{ \AA}^3$. A vacuum shell of 3-5 \AA around the clusters was considered to be a sufficient and reasonable range for AIMD simulations of non-periodic isolated systems.⁴⁷ The Poisson solver wavelet^{48,49} was chosen to solve the Poisson equation to satisfy the non-PBC. This solver is compared to the Martyna-Tuckerman solver⁵⁰ in Sec. S5 in SI. It is noted that this is the first usage of BOMD in capturing the cluster fragmentation and observing directly the motions of several transferable protons in a protonated cluster.

Results and discussion

Charge-induced structural instability

Defining the charge-induced instability in sub-nanometer clusters entails several challenges. Deviations from predictions of linear theories⁷⁻⁹ for the onset of the charge-induced instabilities may arise by the high electric fields applied from the ion in only two-three hydration shells that are present in the sub-nanometer cluster sizes as well as large shape fluctuations relative to the spherical shape inherent in small clusters. In particular, smaller ions such as Fe^{3+} can produce high fields that tightly orient nearby water molecules, limiting their polarizability and disrupting the expected linear dielectric response. Eq. 7 in Ref.⁹ and Eq. 1 in this manuscript come from a linear theory.^{7,9} Because of the lack of a non-linear theory, we employ them to provide an estimate of the cluster size where the instability may manifest. As we will discuss, the simulations show agreement with the theoretical predictions. Equation 7 in Ref.⁹ for a certain value of the dielectric constant, ϵ , of a dielectric droplet containing a single (macro)ion, yields the minimum X by varying the order of the spherical harmonics, l . This value of X is used in Eq. 1 to approximately compute the radius, R , of the droplet and from R the number of H_2O molecules, $N_{\text{H}_2\text{O}}$. Combinations of values of ϵ that vary in the range of 10 to 82, with those of surface tension, γ in the

range of 52.3 mN/m (which is the γ for TIP3P H₂O model⁵¹ at 300 K) to 10 mN/m yields a minimum number of $N_{\text{H}_2\text{O}} = 92$ below which the instability may manifest. A combination of $\epsilon = 10$ and $\gamma = 10$ mN/m yields $N_{\text{H}_2\text{O}} = 242$, which is the prediction for the maximum number of H₂O molecules below which the instability may manifest.

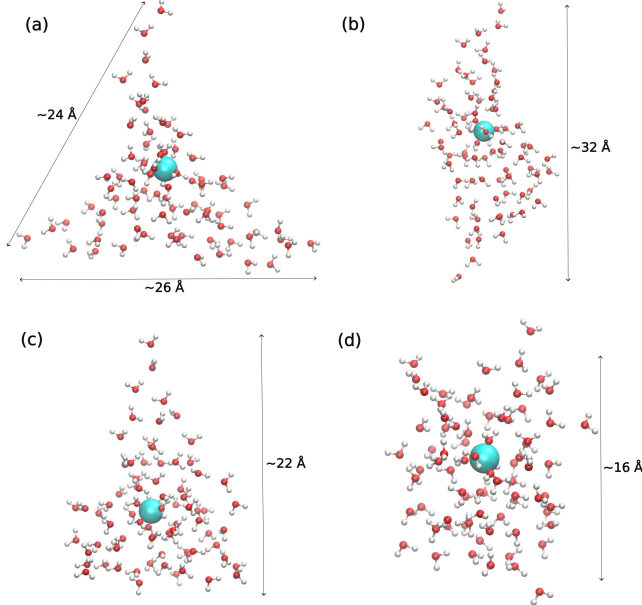


Figure 1: Typical snapshots of a cluster comprised a single Fe^{3+} ion and $N_{\text{H}_2\text{O}} = 78$ at 190 K over 40 ns production run reveal four distinct motifs: (a) triangular, (b) elongated with two diametric conical tips, (c) a single conical tip, and (d) a more spherical with a cleaved surface into several and shorter conical protrusions relative to the triangular shape. The color coding is: turquoise sphere represents the Fe^{3+} ion, red oxygen sites, and white hydrogen sites.

The example of Fe^{3+} is employed to demonstrate the instability and is compared with La^{3+} , and Lu^{3+} . Figure 1 shows typical snapshots of cluster configurations for a Fe^{3+} - $N_{\text{H}_2\text{O}} = 78$ system at 190 K and a Movie in SI shows the transitions. Within the energy landscape, the cluster dynamically evolves through configurations with a triangular (Fig. 1 (a)), elongated with two diametric conical tips (Fig. 1 (b)), one conical tip (Fig. 1 (c)), and a more spherical shape with several and shorter conical protrusions on the surface (Fig. 1 (d))

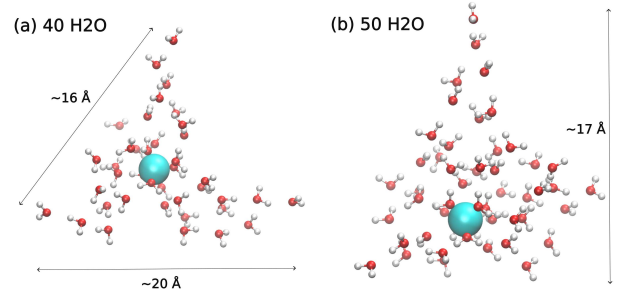


Figure 2: Typical snapshots of clusters comprised a single Fe^{3+} ion and (a) $N_{\text{H}_2\text{O}} = 40$, (b) $N_{\text{H}_2\text{O}} = 50$ at 130 K. The color coding is the same as in Fig. 1.

than the triangular shape. The continuous transition among the shapes is consistent with the fact the physical properties change continuously in clusters as for example in phase transitions.^{1,2} These structures are to be compared with the stable “star-like” shapes that we found^{9,12} in dielectric droplets comprised $N_{\text{H}_2\text{O}} \gtrsim 1000$ and a single macroion such as a nucleic acid or a protein. In a droplet containing $N_{\text{H}_2\text{O}} \gtrsim 1000$ “star-like” shapes with a specific number of points are maintained for a range of droplet sizes as shown in Fig. 2 in Ref.⁹ As the droplet size changes sharp transitions between “star-like”-shapes with a different number of points were observed. Occasionally, very near this transition point a droplet may visit “star-like” configurations with both n and $n + 1$ points. In contrast, in the sub-nanometer sized clusters, we find that “star-like”-shapes with different number of points are explored by the same cluster size at $T = 190$ K where the H₂O molecules are still mobile. These continuous transitions between different shapes may arise from the fact that the large relative shape fluctuations in the clusters lower the energy barrier among the various shapes. Similarly to Fe^{3+} , clusters at $T = 190$ K comprised a single La^{3+} or Lu^{3+} and $N_{\text{H}_2\text{O}} < 100$ show pronounced shape deformations with one, two and three conical protrusions. Interestingly, the prediction of the analytical theory for the minimal number of H₂O molecules below which the structural instability may manifest is in agreement with the

simulation results. For $N_{\text{H}_2\text{O}} > 100$ the number of conical protrusions on the surface attenuate as the cluster size increases.

At $T = 130$ K, the H_2O molecules are immobile. Because of the suppression of the thermal fluctuations it may be expected that a specific “star-like”-shape will appear permanently within a long simulation. Indeed, Fig. 2 for $N_{\text{H}_2\text{O}} = 40$ and 50, shows three-point (Fig. 2 (a)) and one-point (Fig. 2 (b)) “star-like” shapes, respectively that are maintained throughout a simulation of 40 ns. For $N_{\text{H}_2\text{O}} \gtrsim 60$ the shapes do not show large conical deformations on the surface. The cease of the instability earlier than for droplets at 190 K is attributed to the fact that at 130 K the surface tension is higher and the slow dynamics may trap the cluster in certain long-lasting potential energy minima. The considerably slow dynamics of the clusters at the low temperature requires a separate study that we currently perform to identify the emergence of ice-like structures and the relation to instability. Aqueous clusters at 130 K composed of several tens of H_2O molecules and a single La^{3+} or Lu^{3+} ion also show one, two, three or more distinct conical protrusions, similar to Fe^{3+} .

We further investigate the distinct shape fluctuations of the trivalent metal ion clusters in Fig. 3 (a) that shows the shape deviations of clusters comprised $\text{Fe}^{3+}\text{-}N_{\text{H}_2\text{O}} = 70 - 85$ from that of a pristine $N_{\text{H}_2\text{O}} = 70$ cluster and, in Fig. 3 (b) the deviation of clusters comprised $\text{Fe}^{3+}\text{-}N_{\text{H}_2\text{O}} = 150 - 242$ from a pristine cluster comprised $N_{\text{H}_2\text{O}} = 242$. We define a descriptor of the cluster shape by the difference between the largest (I_3) and smallest (I_1) moments of inertia divided by the sum of the three moments of inertia, $I_1 + I_2 + I_3$. This descriptor nearly removes the effect of the cluster size from the comparison of the shapes and as a result we can compare the shapes of different cluster sizes shown in Fig. 3 (a) and (b).

Figure 3 (a) and (b) show that shapes of clusters even with $N_{\text{H}_2\text{O}} \sim 150$ deviate from those of the pristine H_2O clusters. The $N_{\text{H}_2\text{O}} \sim 150$ do not show well-defined conical protrusions as the clusters with $N_{\text{H}_2\text{O}} \lesssim 100$ but they still show pronounced shape fluctuations because of the

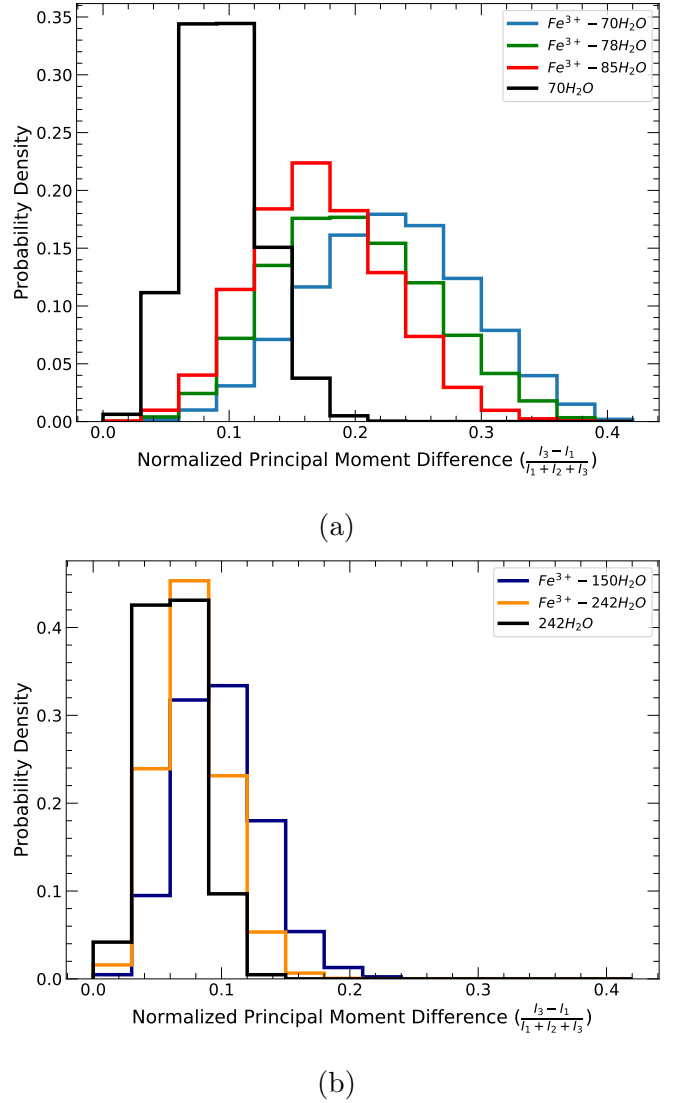


Figure 3: (a) Probability distribution of the ratio of the difference between the largest (I_3) and smallest (I_1) moments of inertia divided by the sum of the three moments of inertia ($I_1 + I_2 + I_3$) in $\text{Fe}^{3+}\text{-}N_{\text{H}_2\text{O}} = 70 - 85$ clusters. A pristine cluster comprised $N_{\text{H}_2\text{O}} = 70$ is used as a reference system. The simulations were performed at $T = 190$ K and the production run was 40 ns. (b) Same as (a) but for $\text{Fe}^{3+}\text{-}N_{\text{H}_2\text{O}} = 150 - 242$ clusters. The reference system is a pristine cluster comprised of $N_{\text{H}_2\text{O}} = 242$.

presence of the ion, that are different from those of a pristine aqueous cluster. The analysis of the cluster shapes suggests that for $N_{\text{H}_2\text{O}} < 242$ the orientation of the H_2O molecules will be influenced by the distinct geometries and shape fluctuations induced by the ion.

Ordering of H₂O molecules

The range of the electric field of the ion shows its imprint in the structure of the H₂O molecules surrounding the ions as it is described in the radial distribution functions (RDFs) and in the orientation of the surrounding H₂O molecules.

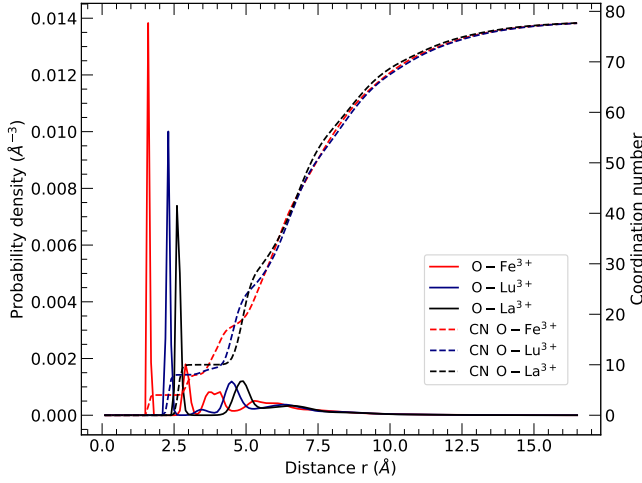


Figure 4: Radial distribution function (RDF) and coordination number between oxygen sites of H₂O and Fe³⁺ ion (red colored), Lu³⁺-O (blue colored), and La³⁺-O (black colored) in $N_{\text{H}_2\text{O}} = 78$ at $T = 190$ K.

The RDFs between the oxygen sites and a trivalent metal ion in $N_{\text{H}_2\text{O}} = 78$ are shown in Fig. 4 at $T = 190$ K. The location of the maxima and the coordination numbers for Fe³⁺-O, La³⁺-O, and Lu³⁺-O in $N_{\text{H}_2\text{O}} = 78$ are summarized in Table S4 in SI. A similar RDF to Fig. 4 (a) but for $N_{\text{H}_2\text{O}} = 242$ is shown in Fig. S4 in SI. As expected, the RDFs indicate more structured hydration shells surrounding Fe³⁺, which is the smallest among the studied ions. The intensity of the first peak for the Fe³⁺-O is distinctly higher than that of Lu³⁺-O and La³⁺-O, which indicates the rigidity in the first hydration shell of Fe³⁺ relative to that of Lu³⁺ and La³⁺. The maximum of the Fe³⁺-O peak is at 1.6 Å, while of Lu³⁺ and La³⁺ at 2.3 Å and 2.6 Å, respectively. It is interesting to note that for Fe³⁺ there are two consecutive peaks between 2.5 Å to 4.5 Å, which indicates that the second and third hydration shells of Fe³⁺ are densely arranged around the Fe³⁺ cen-

ter. Similar structure appears for Lu³⁺ but with lower intensity. For La³⁺, which is the largest ion, only one maximum appears at 4.8 Å. Figure S5 in SI for $N_{\text{H}_2\text{O}} = 40$ at $T = 130$ K, shows a rigid structure within the clusters arising from the immobility of the H₂O at the low temperature.

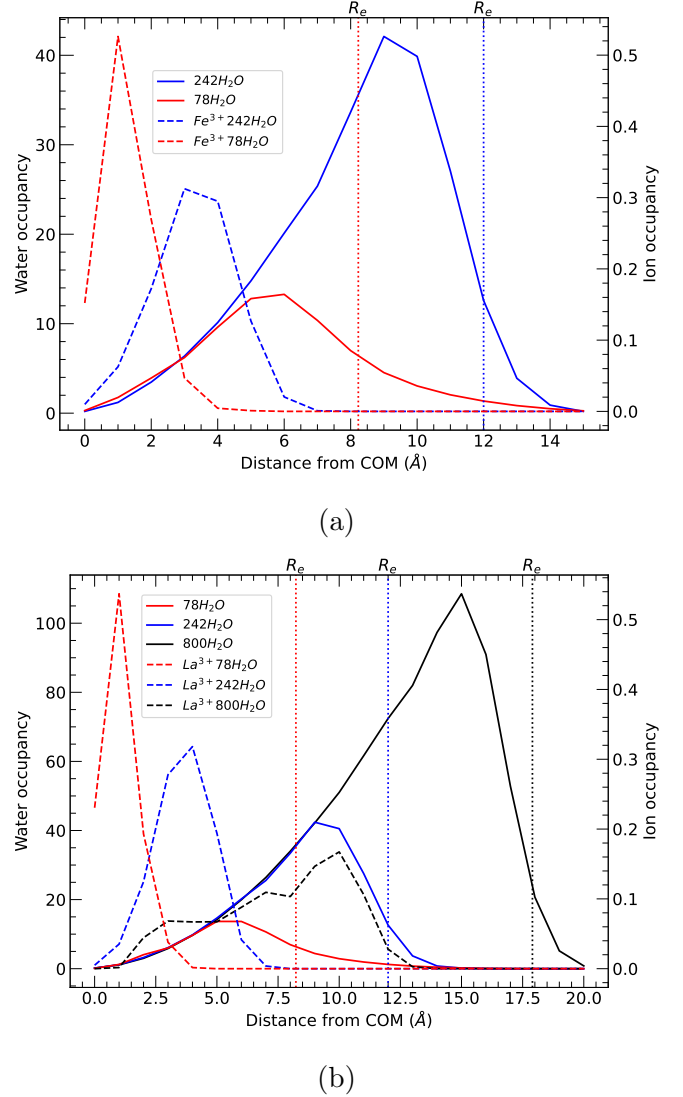


Figure 5: Raw data of the probability of encountering the ion and the H₂O molecules at a certain distance from the cluster's COM. The data have not been divided by the volume element. The vertical dotted lines mark the equimolar radius (R_e) of the cluster. (a) Fe³⁺ in $N_{\text{H}_2\text{O}} = 78, 242$, (b) La³⁺ in $N_{\text{H}_2\text{O}} = 78, 242, 800$.

The orientation of the H₂O molecules is better analyzed when the depth of the ion from the surface of the cluster is known. Figure 5 (a)

shows the raw data of the probability of encountering the ion and the H_2O molecules at a certain distance from the cluster's COM for Fe^{3+} in $N_{\text{H}_2\text{O}} = 78$ and $N_{\text{H}_2\text{O}} = 242$. In $N_{\text{H}_2\text{O}} = 78$, Fe^{3+} is found two hydration layers below the cluster surface while in $N_{\text{H}_2\text{O}} = 242$ the depth is three layers⁵² because of the large available volume. The long tail up to 14.0 Å in the probability of the H_2O in $N_{\text{H}_2\text{O}} = 78$ is a signature of the conical protrusions, while this tail is much shorter in $N_{\text{H}_2\text{O}} = 242$. Similar to Fig. 5 (a), Figure 5 (b) shows that La^{3+} in $N_{\text{H}_2\text{O}} = 242$ and $N_{\text{H}_2\text{O}} = 800$ is found three H_2O layers below the surface.

Figure 6 (a), (b), and (c) show the orientation of the H_2O molecules around Fe^{3+} , Lu^{3+} , and La^{3+} , respectively, for $N_{\text{H}_2\text{O}} = 78$ and $N_{\text{H}_2\text{O}} = 242$. In the first hydration shell of the ion, there is not only a strong local ordering as indicated by the RDFs (Fig. 4) but also strong orientational ordering of the H_2O dipoles where $\theta \sim 180^\circ$ (definition of θ is found in Fig. 6 (a)) as shown in the first segment of Fig. 6 (a), (b), (c).

In the second hydration shell, the orientation becomes rapidly more disordered. As it is expected, the larger the trivalent ion is, the more the randomization towards a zero value of $\langle \cos(\theta) \rangle$ is. In the values of $\cos(\theta)$ within the second hydration shell of the Fe^{3+} and Lu^{3+} we see a distinct peak that corresponds to the two peaks that we see in their RDFs (Fig. 4) between 2.5-4.5 Å for Fe^{3+} and 3.0-5.5 Å for Lu^{3+} . The pattern of H_2O dipole moment orientations follows: the stronger electric field exerted from the ion on the H_2O molecules, the more oscillations of $\langle \cos(\theta) \rangle$ occur. This effect is more pronounced for Fe^{3+} than for Lu^{3+} or La^{3+} . The ion's strong electric field even though decreases in the third hydration shell still persists enough to induce a slight water orientation. In clusters with up to several tens of H_2O molecules, as for example in $N_{\text{H}_2\text{O}} = 78$, the third hydration shell surrounding the ion is frequently not continuous because of the “star”-shaped configurations that form troughs near the ion (see Fig. 1). For La^{3+} and Lu^{3+} the orientation of the H_2O molecules in the third and later hydration shells becomes more organized, while for Fe^{3+} the ori-

entation is obviously more aligned beyond the third hydration shell. The increased orientation beyond the second hydration shell is attributed to the alignment of the H_2O molecules within the conical rays of the star-like shapes. Typical snapshots that show the alignment of the H_2O molecules is shown in Fig 7. In Fig 7, frequently encountered ring structures formed by the H_2O molecules are indicated. Such structures were not as likely to appear in $N_{\text{H}_2\text{O}} = 242$ clusters. As it will be discussed in the next section, in the proxy model system containing three H_3O^+ ions instead of a trivalent metal ion, these ring structures show increased proton diffusion. In $N_{\text{H}_2\text{O}} = 242$ clusters, the degree of disorder in the third hydration shell and beyond is much higher than in $N_{\text{H}_2\text{O}} = 78$ because the instability has ceased in this cluster size. The orientation of the H_2O molecules is not influenced anymore by the formation of the conical shapes but it may be influenced by distinct shape fluctuations as indicated in Fig. 3. An average $\cos(\theta)$ near zero indicates no preferential alignment of water dipoles, reflecting a bulk-like water orientation.

A detailed presentation of the distribution of the $\cos(\theta)$ as a function of the distance from the ion is shown in Fig. 6 (d), (e), and (f) for $N_{\text{H}_2\text{O}} = 242$, while for $N_{\text{H}_2\text{O}} = 78$ is shown in Fig. S6 in SI. In Fig. 6 (d)-(e) distinct maxima in the range 0-6.0 Å are present for the three ions. In the range of 7.5-10.5 Å for Fe^{3+} , and in 8.0-10.5 Å for Lu^{3+} a broad local maximum appears that is not present for La^{3+} . Any of the trivalent metal ions studied here, resides the most of the time approximately three H_2O layers below the cluster surface as shown in Fig. 5. As a result these broad local maxima also include the orientation of surface molecules. The presence of these local maxima are signatures of the the range of the ion's electric field. They indicate that for Fe^{3+} and Lu^{3+} the range of the electric field extends to three hydration shells around the ion.

An analysis of the distribution of the acceptor (A)-donor (D) relation of H_2O molecules using VMD in $N_{\text{H}_2\text{O}} = 78$ at $T = 190$ K shows that relative to pure H_2O clusters, the percentage of ADD and AADD in the metal ion clus-

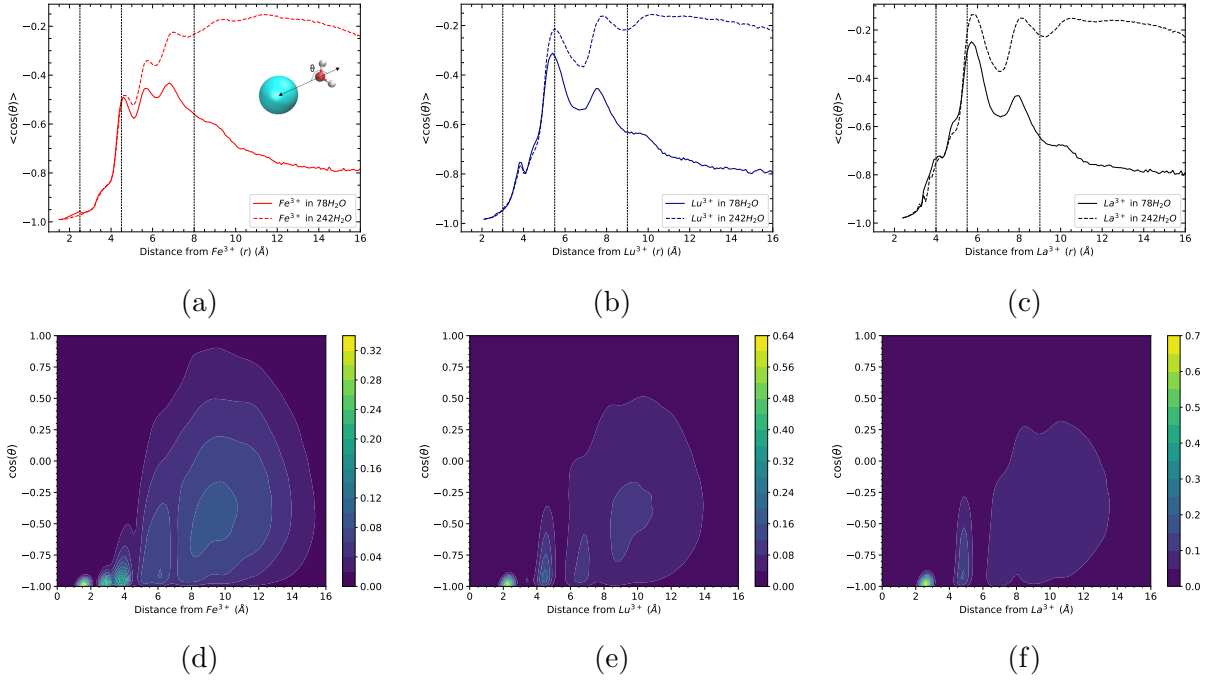


Figure 6: (a)-(c) Average $\cos(\theta)$ as a function of distance (r) from (a) Fe^{3+} , (b) Lu^{3+} , and (c) La^{3+} for $N_{\text{H}_2\text{O}} = 78$ (solid lines) and $N_{\text{H}_2\text{O}} = 242$ (dashed lines) at 190 K. θ is defined as the angle between the dipole moment of a H_2O molecule defined from the negative site to the positive site and a unit vector from the oxygen site of a H_2O molecule to the center of the ion (see inset in (a)). The vertical lines mark the boundaries of the hydration shells as estimated from the RDFs in Fig. 4. (d)-(f) Contour maps of $\cos(\theta)$ distribution of H_2O dipole orientations within successive spherical shells centered at (d) Fe^{3+} , (e) Lu^{3+} , and (f) La^{3+} in $N_{\text{H}_2\text{O}} = 242$ at 190 K. Contour maps for $N_{\text{H}_2\text{O}} = 78$ are shown in Fig. S6 in SI.

ters decreases with decreasing ion size, D, DD, consistently increases with decreasing ion size, while A increases by the same amount for all ion sizes. In the analysis the definition of the H-bond was based on O-O distance equal to 3.2 Å and angle 30°. The decrease of ADD and AADD with decreasing ion size is expected because of the larger disruption of the H-bonded network by the smallest ion, while the increase of D, DD, and A, may reflect the ordering of the H_2O molecules in the conical protrusions.

Based on these findings, we expect the spectrum of Fe^{3+} - H_2O clusters to exhibit a significant red shift in the free-OH band compared to the monovalent and divalent ions studied by Williams et al.,^{15,40} due to the intense electric field of Fe^{3+} . The morphology observed in our simulations, with highly anisotropic structures for small clusters and a transition toward more spherical configurations beyond ~ 100

H_2O molecules, suggests that the intensity and position of the IR bands could vary with cluster size. Specifically, smaller clusters should exhibit a broader and more structured spectrum due to variable solvation environments due to conical protrusions, whereas larger clusters may display a more defined free-OH band shifted to lower energies, reflecting enhanced hydrogen-bond stabilization. Additionally, the bonded-OH band is expected to extend to lower frequencies compared to systems with lower-charge ions, indicating a strong reorganization of the hydrogen-bond network in response to Fe^{3+} electric field. A similar trend is expected for Lu^{3+} and La^{3+} though less pronounced due to their larger ionic radius.

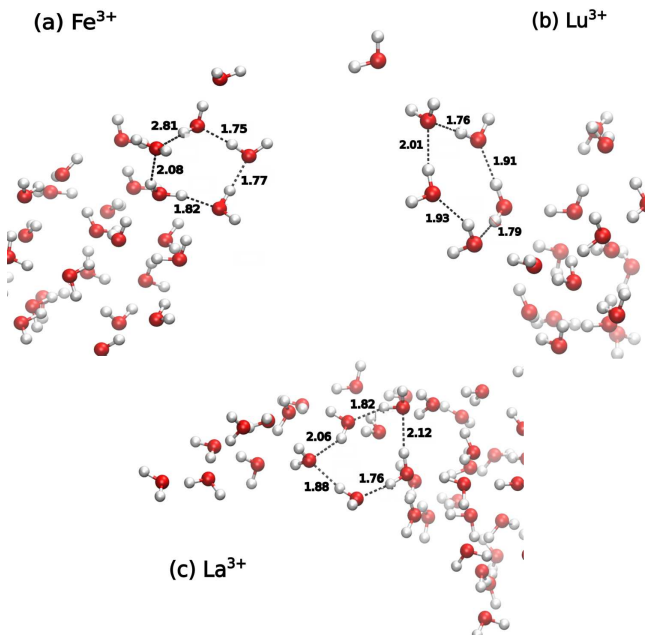


Figure 7: Typical snapshots of the water ring structure in one of the conical protrusions of (a) Fe³⁺, (b) Lu³⁺, and (c) La³⁺ in $N_{\text{H}_2\text{O}} = 78$ at $T = 190$ K. In each snapshot, the lengths of H-bonds are indicated.

Acidity within protruding rings in multi-protonated aqueous clusters

To probe the acidity in the conical protrusions formed by the instability, we employ multi-protonated aqueous clusters as a model system. AIMD is employed which allows for direct observation of proton transfer events. Because of computational efficiency a cluster comprised $N_{\text{H}_2\text{O}} = 64$ and $3\text{H}_3\text{O}^+$ ions is modeled. This cluster is slightly above the Rayleigh limit ($X > 1$ in Eq. 1) and comparable in size with the cluster sizes manifesting instability in the presence of a trivalent ion. A typical snapshot of a $N_{\text{H}_2\text{O}} = 64-3\text{H}_3\text{O}^+$ cluster is shown in Fig. 8 (a). The three H_3O^+ are located on the surface as it has been found for single H_3O^+ ions in clusters.^{53,54} In this cluster an extrusion has been formed on the surface that contains a single H_3O^+ ion. Because of supercharging the cluster is expected to divide easily into two or three sub-clusters, where each of them carries a solvated H_3O^+ ion. Indeed in classical MD we observed fragmentation into three sub-clusters within a few ps. AIMD simulations showed the

$N_{\text{H}_2\text{O}} = 64-3\text{H}_3\text{O}^+$ cluster to be connected with an extruded segment from the body of the cluster. No division of the cluster took place within 7 ps.

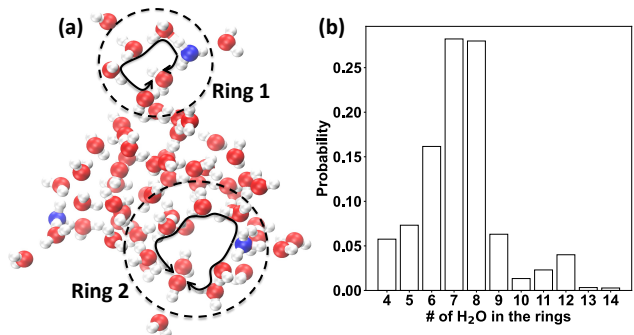


Figure 8: (a) A typical snapshot from the AIMD trajectory of the $64 \text{H}_2\text{O} - 3 \text{H}_3\text{O}^+$ cluster. Oxygen sites of the H_2O molecules are colored red and H sites are white. The O sites of the three H_3O^+ ions are colored blue. Here, the example of two rings (out of three) of different length that contain a single H_3O^+ ion in each of them are shown within the dashed circles. The H_3O^+ ions are characterized by outgoing chains, as indicated by the path marked by the black arrow. The length of ring 1 is 6 containing a single H_3O^+ ion and 5 other H_2O molecules connected with one another by hydrogen bonds. Ring 2 is composed of 8 water molecules, containing a single H_3O^+ ion and 7 other H_2O molecules connected with one another by hydrogen bonds. (b) Distribution of ring sizes around the three H_3O^+ ions.

The difference in the fragmentation time observed between MD with empirical force fields and AIMD may arise from their distinct capabilities in describing intermolecular interactions and the associated cluster dynamics. In “classical” MD simulations, the H_3O^+ ions are typically treated using a rigid water model inherently neglects the effects of electronic polarization and charge redistribution, leading to a weaker and less stable hydrogen bonding network. Consequently, the H_3O^+ ions in classical MD are more prone to cluster fragmentation. By construction, AIMD incorporates the explicit calculation of electronic structure, allowing for dynamic charge transfer, polarization, and hydrogen bond reorganization within

the cluster. These features significantly enhance the structural stability and cohesion of the clusters. Furthermore, the weakness of empirical force fields to inherently capture proton transfer between water molecules contrasts with AIMD, where such processes naturally emerge, contributing to the overall stabilization of the clusters.

Molecular modeling of droplets containing a few tens of thousands of H_2O molecules has shown that near the onset of instability, clusters containing several single ions form conical protrusions on the surface.⁵⁵ The cones formation is governed by the same physical principles as those in the presence of a trivalent ion. The conical protrusions are dynamic, they can form and retract void of any ions, or when a conical deformations forms, an ion at the vicinity of the cone may enter its base and diffuse to the tip from where it is emitted.¹¹ In the $N_{\text{H}_2\text{O}} = 64\text{-}3\text{H}_3\text{O}^+$ cluster the extrusion is maintained within 7 ps of AIMD run. Because of the small size of the cluster modeled by AIMD the extruded segment contains only several H_2O molecules that are highly oriented. Strong orientation of the H_2O molecules has been also found in the conical protrusions in the metal ion clusters at the instability regime as was discussed in Fig. 6 and Fig. 7).

In particular, Fig. 7 shows the formation of ring H-bonded structures observed in the conical regions for the three ions studied here. Similarly, Fig. 8 (b) indicates that in the extruded segment, and around one of the H_3O^+ ions in the more spherical body of the cluster, H_2O molecules form H-bonded rings. The ring structure was determined based on setting up the cutoffs between the O-O distance to 3.2 Å, then the H-O distance to 2.39 Å, and then the hydrogen bonding angle O-H-O to $\geq 155^\circ$. The program runs on the searching rule of all potential proton transfer pathways starting from H_3O^+ ion, then it progressively finds the closed ring step by step using the cutoffs as defined above. To make the ring structure search more efficient, a preliminary search cutoff of 3.5 Å is added. In the way, the present water molecule will search the next candidate water molecule that is likely to participate in ring structure

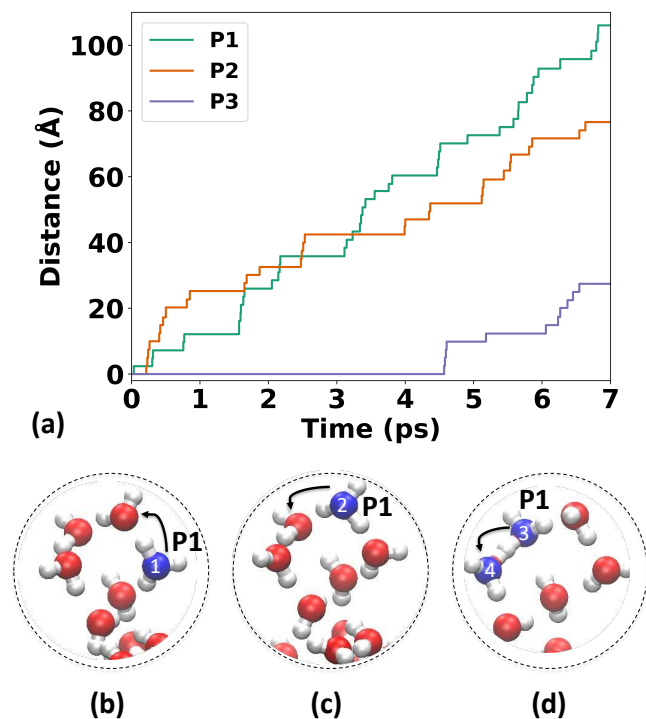


Figure 9: (a) The accumulative distance of proton transfer for three protons (P1-P3) in the $64 \text{ H}_2\text{O}-3 \text{ H}_3\text{O}^+$ system. (b)-(d) Typical snapshots of proton (P1) transfer along the rings were taken from the AIMD simulations. The color coding of the atomic sites is the same as that in Fig. 8. The black dashed circles in (b)-(d) highlight the configuration facilitating the fast proton transfer from oxygen sites of 1 to 4 (colored in blue) within the ring.

within this preliminary region.

It is noted that all ring structures such as those shown in Fig. 8 (a) of rings 1 and 2 can be viewed as rings departing from the H_3O^+ ion, with the black arrows in the figure pointing out the possible pathways for proton transfer. It was also found that the size of the rings around H_3O^+ changed during the simulation. Theoretically, a H_3O^+ ion can exist with three ring structures,^{28,56} each starting with one of the water molecules and ending with one of the neighboring water molecules, forming a closed ring. The rings that more frequently appear in the $N_{\text{H}_2\text{O}} = 64\text{-}3\text{H}_3\text{O}^+$ cluster over the 7 ps AIMD run are mainly composed of 5 to 8 H_2O molecules. This is shown in Fig. 8 (b). Snapshots of longer ring structures with 10 and 12

H₂O molecules are shown in Fig. S7 in SI. Ring structures of H₂O have been identified in previous works by Hassanali et al.²⁸ within the bulk solution. Differently in our study, these rings are found at the surface of the cluster or in the protruding portion. Hassanali et al.²⁸ have argued that the units forming the closed rings are related to the stability of the water network around the protons. The rings that are made up of a smaller number of H₂O molecules (less than 10 found in the work of Ref.²⁸) provide longer trapping time for the proton, while regions of larger rings provide shorter trapping time because more transfer paths become available to the proton due to instability of the larger rings. As it will be discussed the ring structures, mainly pentamers to heptamers, in the cluster promote the proton transfer between two adjacent H₂O molecules and proton diffusion over several H₂O molecules.

To the knowledge of the authors, the acidity in the conical region have not been studied before. Clusters comprised $N_{\text{H}_2\text{O}} = 64$ - $3\text{H}_3\text{O}^+$ show that during ~ 7 ps in their connected form, proton transfer events occur between the H₃O⁺ ion and the neighboring H₂O molecules and proton diffusion over several H₂O molecules. The protons in the $N_{\text{H}_2\text{O}} = 64$ - $3\text{H}_3\text{O}^+$ cluster are labeled as P1, P2, and P3. Fig. 9 shows the cumulative distance that each proton has traveled within 7 ps, including returns to the previous donor H₂O molecule. Distinct dynamics among the protons found in different regions of the cluster is observed. P1, that is found in the protrusion undergoes fast forward and back transfer between two H₂O molecules but also successful transfers that allow it to diffuse 5 H₂O molecules away from its starting H₂O molecule. Snapshots that focus on the region of the cluster where P1 is found is shown in Fig. 9 (b)-(d) and a Movie in SI shows the proton diffusion. P2 also transfers over several 4-5 H₂O molecules away from its parent H₂O molecule, then goes back to the initial starting point after 20-30 fs. P1 and P2 participate in ring structures as shown in Fig. 8 (a)-(b). P3 that is in the more spherical body of the cluster (but still stays on the surface as a pyramid structure with three hy-

drogens facing toward to the cluster’s interior) shows delocalization between only two or three H₂O molecules with many re-crossings and returns to its parent H₂O molecule. Simulations of “star-like” droplets has shown that a death-birth process of the rays may take place.¹² By analogy, one may expect that diffusion of P3 toward the H₂O molecules at the bottle-neck may lead to the retraction of the pentameric ring on the cluster surface, while the ring that contains P2 or P1 may start to protrude.

The proton transfer in the clusters studied here has many of the features that have been already identified in the bulk solution^{18-31,57-63} and liquid H₂O planar interface in contact with the vapor.^{53,54,64-74} Our simulations show significant delocalization of H₃O⁺ ions among neighboring water molecules. Specially, this observation is in agreement with earlier multi-state empirical valence bond simulation studies by Voth and coworkers in aqueous clusters,^{53,73,74} who demonstrated proton transfer delocalization and frequent transitions between Zundel and Eigen complexes. P3 shows frequent proton delocalization over two or three H₂O molecules on the surface corresponding to H₅O₂⁺ (Zundel) and the H₇O₃⁺ (chain) complexes. In addition, the interconversion between the H₉O₄⁺ (Eigen) and H₅O₂⁺ (Zundel) complexes near the surface of the clusters were observed because a central H₃O⁺ in the Eigen complex randomly approaches one of the three neighboring H₂O molecules during simulations. In this way, the proton transfer between one H₃O⁺ and one H₂O on the surface of the clusters follows the Eigen-Zundel-Eigen mobility mechanism³¹ and was found by Markovitch et al. on the excess proton in the bulk solution using Car-Parrinello MD simulations.

In summary, it was demonstrated that ring structures in protonated clusters assist proton transfer and diffusion. Formation of rings was frequently found in the conical protrusions around Fe³⁺, Lu³⁺, or La³⁺ when a cluster is at the instability regime. The facile proton transfer through the rings suggests higher acidity in the conical regions. Moreover, the frequent proton delocalization within ~ 7 ps of AIMD simulation suggests that a more realistic coarse-

grained model of H_3O^+ ion in modeling H_3O^+ -macromolecule interactions in droplets may include the delocalization of the proton charge over 2 or 3 H_2O molecules.

Conclusion

We addressed the following key questions: (a) How does charge-induced instability manifest in sub-nanometer-sized aqueous clusters charged with a single trivalent metal ion? (b) How do the electric field of the metal ion and the cluster geometry (e.g., conical features) influence the orientation of surrounding H_2O molecules? (c) What is the acidity of water molecules located in the conical protrusions on the surface of the cluster?

The first question explores how a fundamental physical phenomenon—charge-induced instability—transitions from minute nanoscopic systems, where macroscopic theories typically fail, to microscopic behavior. Our simulations revealed that aqueous clusters charged with a trivalent ion in the instability regime acquire morphologies with multiple conical protrusions on their surfaces. The number of protrusions decreases progressively with increasing cluster size. Unlike mesoscopic and microscopic droplets—where ‘star-like’ shapes transition sharply with droplet radius—the shape transitions in sub-nanometer clusters occur continuously. The cluster evolves through triangular, elongated two-point, single-point, and more spherical configurations, often exhibiting surface cones along the way. We propose that the continuous nature of these shape transitions stems from the large relative shape fluctuations in sub-nanometer clusters, which reduce the energy barriers between different configurations. The ion size also influences cluster morphology: for example, for a fixed number of H_2O molecules, Fe^{3+} -containing clusters more frequently adopt elongated two-point configurations, whereas La^{3+} -containing clusters favor single-point structures.

We found that the electric field of the trivalent ion, regardless of its size, strongly influences its immediate two hydration shells. Furthermore,

for clusters undergoing instability, the collective electric field from the ion and surrounding H_2O molecules beyond the second hydration shell strongly orients the H_2O molecules, in contrast to those in clusters that are not subject to instability. In clusters where instability effects have subsided, the trivalent ion is located approximately three hydration shells below the surface. The orientation of the third hydration shell—which includes surface H_2O molecules—is differently influenced by Fe^{3+} , Lu^{3+} , and La^{3+} , depending on the ion’s size.

The cluster morphologies observed in our simulations—featuring highly anisotropic structures in small clusters and a transition toward spherical configurations beyond 100 H_2O molecules—suggest specific trends in their infrared (IR) spectra. Smaller clusters are expected to exhibit broader and more structured spectra due to multiple hydration environments, while larger clusters may display a sharper free-OH band that is red-shifted due to enhanced hydrogen bonding. Furthermore, the bonded-OH band is predicted to extend to lower frequencies compared to clusters containing monovalent or divalent cations, reflecting the strong field-induced reorganization of the hydrogen-bond network by Fe^{3+} .

One limitation of this study is the lack of explicit electronic polarization in the empirical models. However, we addressed this by examining a variety of trivalent ions (Fe^{3+} , Lu^{3+} , La^{3+}), all of which exhibited similar instability behavior. This consistency suggests that the observed phenomena—particularly the shape instability and the positioning of the ion approximately three water layers below the surface—are robust and should persist in simulations using more advanced models that include electronic polarization.

The charge-induced instability shapes are characterized by conical protrusions on the cluster surface. We found that the conical protrusions often host H-bonded pentameric rings. For the first time, the ability of H_2O molecules to facilitate proton transfer in the conical protrusions was examined here. To probe the acidity in the conical regions, we performed ab initio molecular dynamics (AIMD) simulations on

a cluster consisting of 64 H₂O molecules and three H₃O⁺ ions. Pentameric to heptameric rings were clearly identified in the protonated cluster serving as centers for proton diffusion. These calculation suggest that within the conical regions, protons are able to diffuse across several water molecules, unlike the more localized proton delocalization observed in the compact body of the cluster. Moreover, AIMD simulations suggest that electronic polarization and charge transfer processes delay cluster fragmentation relative to predictions based on empirical force fields.

By analogy, we expect clusters containing trivalent metal ions to exhibit enhanced proton delocalization and greater acidity in the conical protrusions at the surface. Whether this behavior persists in larger conical protrusions—such as those formed in Rayleigh jets—remains an open question. Notably, the internal electric field present in such jets due to their dielectric properties can orient water molecules in ways that potentially alter their acid–base characteristics relative to those in the spherical body of the droplet. We hypothesize that this localized enhancement of acidity may facilitate the charging of analytes and macromolecules entrained within the jet during electrospray ionization. As such, our findings offer insight into the fundamental mechanisms of charge transfer and cluster stability at the nanoscale and may have broader implications for analytical techniques like mass spectrometry.

Acknowledgement SC is grateful to Prof. D. Frenkel, Yusuf Hamied Department of Chemistry, University of Cambridge, UK, Prof. R. Kapral, Department of Chemistry, The University of Toronto, Prof. S.S. Xantheas, Pacific Northwest National Laboratory and Dr. Anatoly Malevanets for discussions on the stability of charged systems. SC acknowledges an NSERC-Discovery grant (Canada) for funding this research. MPA acknowledges a MITACS-Globalink internship fellowship held in the SC group. HN acknowledges the province of Ontario and The University of Western Ontario for an Ontario Graduate Scholarship. Digital Research Alliance of Canada is acknowledged for

providing the computing facilities and technical support to perform this research.

Supporting Information

(S1) Models and parameters for MD simulations. (S2) System preparation for AIMD. (S3) AIMD Simulation details. (S4) Protocol validation for AIMD parameters by testing them in bulk solution simulations. (S5) Selection of the Poisson solver. (S6) Radial distribution functions between oxygen and Fe³⁺, Lu³⁺, and La³⁺ in aqueous clusters. (S7) Distribution of $\cos(\theta)$ around Fe³⁺, Lu³⁺, or La³⁺ in aqueous clusters. (S8) Ring structures in clusters comprising 64 H₂O-3H₃O⁺ ions studied by AIMD. (S9) Movie that shows the transitions among different “star-like” shapes for Fe³⁺-N_{H₂O} = 78 at 190 K. (S10) Movie that shows the proton transfer in N_{H₂O} = 64-3H₃O⁺ in AIMD simulation.

Supporting Information Available

The AIMD data supporting this work are available at the University of Western Ontario research data repository, Borealis, at <https://doi.org/10.5683/SP3/3X3Q4D>. The data for La³⁺, Fe³⁺, Lu³⁺, and pure H₂O are available at <https://doi.org/10.7910/DVN/6FGMZS>, <https://doi.org/10.7910/DVN/MH3AXZ>, <https://doi.org/10.7910/DVN/DHOTEX>, and <https://doi.org/10.7910/DVN/FWB7K2>, respectively.

Author Contributions

First authorship is equally shared between JS and HN. MPA contribution: editing of the manuscript, production and analysis of data, assistance with the usage of software, literature analysis. SC contribution: Conceptualization (100%), acquiring funding (100%), writing and editing of the manuscript, formal data analysis,

literature review and analysis, supervision and communication, handling of submission.

References

- (1) Berry, R. S.; Wales, D. J. Freezing, melting, spinodals, and clusters. *Phys. Rev. Lett.* **1989**, *63*, 1156.
- (2) de With, G. Melting is well-known, but is it also well-understood? *Chem. Rev.* **2023**, *123*, 13713–13795.
- (3) Signorell, R.; Winter, B. Photoionization of the aqueous phase: clusters, droplets and liquid jets. *Phys. Chem. Chem. Phys.* **2022**, *24*, 13438–13460.
- (4) Gilligan, J.; Castleman, A. *Water in confining geometries*; Springer, 2003; pp 101–135.
- (5) Burnham, C. J.; Petersen, M. K.; Day, T. J.; Iyengar, S. S.; Voth, G. A. The properties of ion-water clusters. II. Solvation structures of Na⁺, Cl⁻, and H⁺ clusters as a function of temperature. *J. Chem. Phys.* **2006**, *124*, 024327.
- (6) Stuart, S. J.; Berne, B. Effects of polarizability on the hydration of the chloride ion. *J. Phys. Chem.* **1996**, *100*, 11934–11943.
- (7) Rayleigh, L. XX. On the equilibrium of liquid conducting masses charged with electricity. *Philos. Mag.* **1882**, *14*, 184–186.
- (8) Hendricks, C.; Schneider, J. Stability of a conducting droplet under the influence of surface tension and electrostatic forces. *Am. J. Phys.* **1963**, *31*, 450–453.
- (9) Oh, M. I.; Malevanets, A.; Paliy, M.; Frenkel, D.; Consta, S. When droplets become stars: charged dielectric droplets beyond the Rayleigh limit. *Soft Matter* **2017**, *13*, 8781–8795.
- (10) Duft, D.; Achtzehn, T.; Müller, R.; Huber, B. A.; Leisner, T. Rayleigh jets from levitated microdroplets. *Nature* **2003**, *421*, 128–128.
- (11) Consta, S. Atomistic modeling of jet formation in charged droplets. *J. Phys. Chem. B* **2022**, *126*, 8350–8357.
- (12) Consta, S. Manifestation of Rayleigh instability in droplets containing multiply charged macroions. *J. Phys. Chem. B* **2010**, *114*, 5263–5268.
- (13) Sharawy, M.; Consta, S. Characterization of “star” droplet morphologies induced by charged macromolecules. *The Journal of Physical Chemistry A* **2016**, *120*, 8871–8880.
- (14) Kim, D.; Wagner, N.; Wooding, K.; Clemmer, D. E.; Russell, D. H. Ions from solution to the gas phase: a molecular dynamics simulation of the structural evolution of substance P during desolvation of charged nanodroplets generated by electrospray ionization. *J. Am. Chem. Soc.* **2017**, *139*, 2981–2988.
- (15) Prell, J. S.; O’Brien, J. T.; Williams, E. R. Structural and electric field effects of ions in aqueous nanodrops. *J. Am. Chem. Soc.* **2011**, *133*, 4810–4818.
- (16) O’Brien, J. T.; Williams, E. R. Effects of ions on hydrogen-bonding water networks in large aqueous nanodrops. *Journal of the American Chemical Society* **2012**, *134*, 10228–10236.
- (17) Yang, N.; Duong, C. H.; Kelleher, P. J.; McCoy, A. B.; Johnson, M. A. Deconstructing water’s diffuse OH stretching vibrational spectrum with cold clusters. *Science* **2019**, *364*, 275–278.
- (18) DeCoursey, T. E.; Hosler, J. Philosophy of voltage-gated proton channels. *J. R. Soc. Interface.* **2014**, *11*, 20130799.
- (19) Natzle, W. C.; Moore, C. B. Recombination of hydrogen ion (H⁺) and hydroxide

- in pure liquid water. *J. Phys. Chem.* **1985**, *89*, 2605–2612.
- (20) Hückel, E. 3. Einzelvorträge: elektrochemie. theorie der beweglichkeiten des wasserstoff-und hydroxylions in wässriger lösung. *Zeitschrift für Elektrochemie und angewandte physikalische Chemie* **1928**, *34*, 546–562.
 - (21) De Grotthuss, C. Sur la décomposition de l’eau et des corps qu’elle tient en dissolution à l’aide de l’électricité galvanique. *Ann. chim* **1806**, *58*, 54.
 - (22) Cukierman, S. Et tu, Grotthuss! and other unfinished stories. *Biochim. Biophys. Acta, Bioenerg.* **2006**, *1757*, 876–885.
 - (23) Agmon, N. The grotthuss mechanism. *Chem. Phys. Lett.* **1995**, *244*, 456–462.
 - (24) Agmon, N.; Bakker, H. J.; Campen, R. K.; Henchman, R. H.; Pohl, P.; Roke, S.; Thämer, M.; Hassanali, A. Protons and hydroxide ions in aqueous systems. *Chem. Rev.* **2016**, *116*, 7642–7672.
 - (25) Geissler, P. L.; Dellago, C.; Chandler, D.; Hutter, J.; Parrinello, M. Autoionization in liquid water. *Science* **2001**, *291*, 2121–2124.
 - (26) Brewer, M. L.; Schmitt, U. W.; Voth, G. A. The formation and dynamics of proton wires in channel environments. *Biophys. J.* **2001**, *80*, 1691–1702.
 - (27) Hassanali, A.; Prakash, M. K.; Eshet, H.; Parrinello, M. On the recombination of hydronium and hydroxide ions in water. *Proc. Natl. Acad. Sci. U.S.A.* **2011**, *108*, 20410–20415.
 - (28) Hassanali, A.; Giberti, F.; Cuny, J.; Kühne, T. D.; Parrinello, M. Proton transfer through the water gossamer. *Proc. Natl. Acad. Sci. U.S.A.* **2013**, *110*, 13723–13728.
 - (29) Tuckerman, M.; Laasonen, K.; Sprik, M.; Parrinello, M. Ab initio molecular dynamics simulation of the solvation and transport of H₃O⁺ and OH⁻ ions in water. *J. Phys. Chem.* **1995**, *99*, 5749–5752.
 - (30) Newton, M.; Ehrenson, S. Ab initio studies on the structures and energetics of inner-and outer-shell hydrates of the proton and the hydroxide ion. *J. Am. Chem. Soc.* **1971**, *93*, 4971–4990.
 - (31) Markovitch, O.; Chen, H.; Izvekov, S.; Paesani, F.; Voth, G. A.; Agmon, N. Special pair dance and partner selection: Elementary steps in proton transport in liquid water. *J. Phys. Chem. B* **2008**, *112*, 9456–9466.
 - (32) Saha, R.; Mitra, R. K. Trivalent cation-induced phase separation in proteins: ion specific contribution in hydration also counts. *Phys. Chem. Chem. Phys.* **2022**, *24*, 23661–23668.
 - (33) Beyer, M. K. Hydrated metal ions in the gas phase. *Mass Spectrom. Rev.* **2007**, *26*, 517–541.
 - (34) Böhme, D. K.; Schwarz, H. Gas-phase catalysis by atomic and cluster metal ions: the ultimate single-site catalysts. *Angew. Chem., Int. Ed. Engl.* **2005**, *44*, 2336–2354.
 - (35) van der Linde, C.; Ončák, M.; Cunningham, E. M.; Tang, W. K.; Siu, C.-K.; Beyer, M. K. Surface or Internal Hydration—Does It Really Matter? *J. Am. Soc. Mass Spectrom.* **2023**, *34*, 337–354.
 - (36) Yang, F.; Armentrout, P. Periodic trends in the hydration energies and critical sizes of alkaline earth and transition metal dication water complexes. *Mass Spectrom. Rev.* **2025**, *44*, 135–153.
 - (37) Carnegie, P. D.; Marks, J. H.; Brathwaite, A. D.; Ward, T. B.; Duncan, M. A. Microsolvation in V⁺ (H₂O)_n clusters

- studied with selected-ion infrared spectroscopy. *J. Phys. Chem. A* **2020**, *124*, 1093–1103.
- (38) Miliordos, E.; Xantheas, S. S. Elucidating the mechanism behind the stabilization of multi-charged metal cations in water: a case study of the electronic states of microhydrated Mg $2+$, Ca $2+$ and Al $3+$. *Phys. Chem. Chem. Phys.* **2014**, *16*, 6886–6892.
- (39) Armentrout, P.; Beauchamp, J. The chemistry of atomic transition-metal ions: insight into fundamental aspects of organometallic chemistry. *Acc. Chem. Res.* **1989**, *22*, 315–321.
- (40) Bush, M. F.; Saykally, R. J.; Williams, E. R. Reactivity and infrared spectroscopy of gaseous hydrated trivalent metal ions. *J. Am. Chem. Soc.* **2008**, *130*, 9122–9128.
- (41) Cooper, R. J.; DiTucci, M. J.; Chang, T. M.; Williams, E. R. Delayed onset of crystallinity in ion-containing aqueous nanodrops. *J. Am. Chem. Soc.* **2016**, *138*, 96–99.
- (42) Phillips, J. C.; Hardy, D. J.; Maia, J. D. C.; Stone, J. E.; Ribeiro, J. V.; Bernardi, R. C.; Buch, R.; Fiorin, G.; Hénin, J.; Jiang, W. et al. Scalable molecular dynamics on CPU and GPU architectures with NAMD. *J. Chem. Phys.* **2020**, *153*, 044130.
- (43) Humphrey, W.; Dalke, A.; Schulten, K. VMD – Visual Molecular Dynamics. *J. Mol. Graph.* **1996**, *14*, 33–38.
- (44) MacKerell Jr, A. D.; Bashford, D.; Bellott, M.; Dunbrack Jr, R. L.; Evanseck, J. D.; Field, M. J.; Fischer, S.; Gao, J.; Guo, H.; Ha, S. et al. All-atom empirical potential for molecular modeling and dynamics studies of proteins. *J. Phys. Chem. B* **1998**, *102*, 3586–3616.
- (45) Won, Y. Force field for monovalent, divalent, and trivalent cations developed under the solvent boundary potential. *J. Phys. Chem. A* **2012**, *116*, 11763–11767.
- (46) Kühne, T. D.; Iannuzzi, M.; Del Ben, M.; Rybkin, V. V.; Seewald, P.; Stein, F.; Laino, T.; Khaliullin, R. Z.; Schütt, O.; Schiffmann, F. et al. CP2K: An electronic structure and molecular dynamics software package-Quickstep: Efficient and accurate electronic structure calculations. *J. Chem. Phys.* **2020**, *152*, 194103.
- (47) Marx, D.; Hutter, J. *Ab initio molecular dynamics: basic theory and advanced methods*; Cambridge University Press, 2009.
- (48) Genovese, L.; Deutsch, T.; Neelov, A.; Goedecker, S.; Beylkin, G. Efficient solution of Poisson’s equation with free boundary conditions. *J. Chem. Phys.* **2006**, *125*, 074105.
- (49) Genovese, L.; Deutsch, T.; Goedecker, S. Efficient and accurate three-dimensional Poisson solver for surface problems. *J. Chem. Phys.* **2007**, *127*, 054704.
- (50) Martyna, G. J.; Tuckerman, M. E. A reciprocal space based method for treating long range interactions in ab initio and force-field-based calculations in clusters. *J. Chem. Phys.* **1999**, *110*, 2810–2821.
- (51) Vega, C.; de Miguel, E. Surface tension of the most popular models of water by using the test-area simulation method. *J. Chem. Phys.* **2007**, *126*, 154707.
- (52) Ng, K. C.; Adel, T.; Lao, K. U.; Varnecky, M. G.; Liu, Z.; Arrad, M.; Allen, H. C. Iron (III) chloro complexation at the air–aqueous FeCl₃ interface via second harmonic generation spectroscopy. *J. Phys. Chem. C* **2022**, *126*, 15386–15396.
- (53) Petersen, M. K.; Iyengar, S. S.; Day, T. J.; Voth, G. A. The hydrated proton at the water liquid/vapor interface. *J. Phys. Chem. B* **2004**, *108*, 14804–14806.

- (54) Zhang, P.; Feng, M.; Xu, X. Double-layer distribution of hydronium and hydroxide ions in the air–water interface. *ACS Phys. Chem. Au* **2024**, *4*, 336–346.
- (55) Kwan, V.; Consta, S. Conical shape fluctuations determine the rate of ion evaporation and the emitted cluster size distribution from multicharged droplets. *J. Phys. Chem. A* **2022**, *126*, 3229–3238.
- (56) Wu, Y.; Chen, H.; Wang, F.; Paesani, F.; Voth, G. A. An improved multistate empirical valence bond model for aqueous proton solvation and transport. *J. Phys. Chem. B* **2008**, *112*, 467–482.
- (57) Tuckerman, M.; Laasonen, K.; Sprik, M.; Parrinello, M. Ab initio simulations of water and water ions. *J. Phys. Condens. Matter* **1994**, *6*, A93.
- (58) Lobaugh, J.; Voth, G. A. The quantum dynamics of an excess proton in water. *J. Chem. Phys.* **1996**, *104*, 2056–2069.
- (59) Marx, D. Proton transfer 200 years after von Grotthuss: Insights from ab initio simulations. *ChemPhysChem* **2006**, *7*, 1848–1870.
- (60) Calio, P. B.; Li, C.; Voth, G. A. Resolving the structural debate for the hydrated excess proton in water. *J. Am. Chem. Soc.* **2021**, *143*, 18672–18683.
- (61) Eigen, M. Proton transfer, acid-base catalysis, and enzymatic hydrolysis. Part I: elementary processes. *Angew. Chem., Int. Ed. Engl.* **1964**, *3*, 1–19.
- (62) Zundel, G. Hydration structure and intermolecular interaction in polyelectrolytes. *Angew. Chem., Int. Ed. Engl.* **1969**, *8*, 499–509.
- (63) Berkelbach, T. C.; Lee, H.-S.; Tuckerman, M. E. Concerted hydrogen-bond dynamics in the transport mechanism of the hydrated proton: A first-principles molecular dynamics study. *Phys. Rev. Lett.* **2009**, *103*, 238302.
- (64) Vácha, R.; Buch, V.; Milet, A.; Devlin, J. P.; Jungwirth, P. Autoionization at the surface of neat water: is the top layer pH neutral, basic, or acidic? *Phys. Chem. Chem. Phys.* **2007**, *9*, 4736–4747.
- (65) Vácha, R.; Rick, S. W.; Jungwirth, P.; de Beer, A. G.; de Aguiar, H. B.; Samson, J.-S.; Roke, S. The orientation and charge of water at the hydrophobic oil droplet–water interface. *J. Am. Chem. Soc.* **2011**, *133*, 10204–10210.
- (66) Winter, B.; Faubel, M.; Vácha, R.; Jungwirth, P. Behavior of hydroxide at the water/vapor interface. *Chem. Phys. Lett.* **2009**, *474*, 241–247.
- (67) Ottosson, N.; Cwiklik, L.; Soderstrom, J.; Bjorneholm, O.; Ohrwall, G.; Jungwirth, P. Increased Propensity of Iaq⁻ for the Water Surface in Non-Neutral Solutions: Implications for the Interfacial Behavior of H₃Oaq⁺ and OHaq⁻. *J. Phys. Chem. Lett.* **2011**, *2*, 972–976.
- (68) Mishra, H.; Enami, S.; Nielsen, R. J.; Stewart, L. A.; Hoffmann, M. R.; Goddard III, W. A.; Colussi, A. J. Brønsted basicity of the air–water interface. *Proc. Natl. Acad. Sci. U.S.A.* **2012**, *109*, 18679–18683.
- (69) Hub, J. S.; Wolf, M. G.; Coleman, C.; van Maaren, P. J.; Groenhof, G.; van der Spoel, D. Thermodynamics of hydronium and hydroxide surface solvation. *Chem. Sci.* **2014**, *5*, 1745–1749.
- (70) Wick, C. D.; Dang, L. X. Investigating hydroxide anion interfacial activity by classical and multistate empirical valence bond molecular dynamics simulations. *J. Phys. Chem. A* **2009**, *113*, 6356–6364.
- (71) Baer, M. D.; Kuo, I.-F. W.; Tobias, D. J.; Mundy, C. J. Toward a unified picture of the water self-ions at the air–water interface: A density functional theory perspective. *J. Phys. Chem. B* **2014**, *118*, 8364–8372.

- (72) Mundy, C. J.; Kuo, I.-F. W.; Tuckerman, M. E.; Lee, H.-S.; Tobias, D. J. Hydroxide anion at the air–water interface. *Chem. Phys. Lett.* **2009**, *481*, 2–8.
- (73) Iuchi, S.; Chen, H.; Paesani, F.; Voth, G. A. Hydrated excess proton at water- hydrophobic interfaces. *J. Phys. Chem. B* **2009**, *113*, 4017–4030.
- (74) Kumar, R.; Knight, C.; Voth, G. A. Exploring the behaviour of the hydrated excess proton at hydrophobic interfaces. *Faraday Discuss.* **2013**, *167*, 263–278.

Supporting Information:

**From Spheres to Cones: Structural Instabilities
and Acidity at Conical Regions in Trivalent Metal
Ion Nano-clusters**

Jihong Shi, Han Nguyen, Mateo Pescador Arboleda, and Styliani Consta*

Department of Chemistry, The University of Western Ontario, London, Ontario, Canada

N6A 5B7

E-mail: sconstas@uwo.ca

S1. Models and parameters for MD simulations

Molecular dynamics (MD) simulations of aqueous clusters charged by a single Fe^{3+} , Lu^{3+} , and La^{3+} , were performed using the Nanoscale Molecular Dynamics^{S1} (NAMD) v 2.14 software and visualized by Visual Molecular Dynamics^{S2} (VMD) v 1.9.4. The clusters were comprised of $N_{\text{H}_2\text{O}} = 32 - 242$ H_2O molecules. MD simulations were also performed for pristine aqueous clusters with $N_{\text{H}_2\text{O}} = 70$ and 242 for using them as reference systems. For $32 < N_{\text{H}_2\text{O}} < 100$ the cluster sizes were in increments of approximately five H_2O molecules and in particular in the range of $75 < N_{\text{H}_2\text{O}} < 80$ where we were searching for the Rayleigh limit, in increments of one molecule. The water molecules were modelled by the TIP3P-CHARMM model^{S3} and the ions by the parameters reported in Ref.^{S4} Rigid three sites water model has been used extensively in the modeling of Fe^{2+} or Fe^{3+} ions in aqueous systems.^{S5-S8}

The MD simulations of clusters were performed in the canonical ensemble by placing the cluster to the center of a spherical cavity where the spherical boundary condition was applied. The center of mass (COM) of the cluster was restrained to the center of a spherical cavity. The restrain of the COM was applied by using the collective variables module, COLVARS.^{S9} The radius of the cavity was set to three times the radius of the cluster, which ensures a sufficient volume to accommodate any large droplet deformations, such as the formation of conical protrusions. The electrostatic interactions were treated with the multi-level summation method^{S10} (MSM) as implemented in NAMD. In the MSM, a standard cutoff of 12 Å, with a switch distance of 8 Å, and a pairlistdist of 13.5 Å were employed. The choice of default grid spacing 2.5 Å was applied.

The MD runs were performed with the velocity Verlet^{S11} integrator using a time step of 1 fs at temperature $T = 90$ K, 130 K, 190 K and 250 K. The length of the simulation runs was 40 ns. The temperature of the systems was controlled with the Langevin thermostat where the damping coefficient in the Langevin thermostat applied on all atoms was 1 ps. Among the tested temperatures, $T = 190$ K was selected to perform the majority of the simulations. This temperature was selected because at this temperature the molecules in the clusters are

still diffusing within the simulation time. At $T = 90$ K and 130 K the clusters demonstrate deformations caused by the instability but there is no internal motion of the H_2O molecules and the ion within the simulation time.

S2. System preparation for AIMD

Aqueous clusters containing $N_{\text{H}_2\text{O}} = 64$ and $3\text{H}_3\text{O}^+$ ions were prepared using the Packmol package^{S12} and initially simulated with empirical force fields in the large-scale atomic/molecular massively parallel simulator (LAMMPS) package^{S13} version Sep 15, 2022. MD simulation was performed in a simulation cell with dimensions $48 \times 48 \times 48 \text{ \AA}^3$ using the Nosé-Hoover thermostat to set the temperature at 250 K.

In $N_{\text{H}_2\text{O}} = 64$ the three H_3O^+ ions were placed in an isosceles triangle configuration. Two of the ions were placed diametrically apart at a distance of 11.2 \AA and the third one at a distance of 7.92 \AA apart from each of the other two H_3O^+ ions.

The water molecules were modelled by the SPC/Fw^{S14} force field. The empirical force field^{S15,S16} for the H_3O^+ ion were taken from Ref.^{S16} The MSM^{S10,S17} was used to treat the electrostatic interactions. In the implementation of MSM in LAMMPS, the charged cluster was neutralized by evenly placing 40 counter ions (with net charge of -0.0705) at the outermost circle region (with thickness of 10 \AA) in the simulation box to compensate the system charge of $+3$. A command of `kpace-style msm/cg 0.35` was used to set up the cutoff of the atom with the net charge below the $= 0.35$ would not be considered in the calculation of long range electrostatics. The cluster fragmented within 3-5 ps of an MD run. Configurations before the fragmentation were collected as starting configuration in a AIMD simulation in the CP2K software^{S18} v 9.1. The details of the CP2K simulations are discussed in the next section.

S3. AIMD Simulation details

Ab initio MD simulations were performed to study the cluster stability and possible proton transfer in these systems. All calculations were conducted using the electronic structure module Quickstep in the CP2K v 9.1 software package.^{S18} The propagation of the classical nuclei was performed using *ab initio* Born-Oppenheimer MD with a 0.5 fs timestep. At each step of the MD, the electronic orbitals were fine-tuned to the Born-Oppenheimer surface using an orbital transformation method^{S19} with a convergence criterion of 1×10^{-7} a.u.. The conjugate gradient minimizer was employed within the orbital transformation method to perform the optimization. The Gaussian and plane waves method^{S20} expanded the wave function in the Gaussian double-zeta valence polarized (DZVP) basis set.^{S21} Auxiliary plane waves were employed to expand the electron density up to a cutoff of 400 Ry. Two density functional approximations, Perdew-Burke-Ernzerhof (PBE)^{S22} and Becke-Lee-Yang-Parr (BLYP),^{S23,S24} were used with Grimme dispersion corrections^{S25} denoted as D3 here. Adopting empirical dispersion correction to density functionals has shown superiority in optimizing water properties at ambient conditions.^{S26} Goedecker-Teter-Hutter pseudopotentials were utilized to effectively handle the core electrons.^{S27} All the protonated clusters were placed in a large vacuum box of dimensions $48 \times 48 \times 48 \text{ \AA}^3$. A vacuum shell of 3-5 \AA around the clusters was considered to be a sufficient and reasonable range for AIMD simulations of non-periodic isolated systems.^{S28} The Poisson solver WAVELET^{S29,S30} was chosen to solve the Poisson equation to satisfy the non-PBC.

Validation of the AIMD simulation protocol for clusters and to assess the sensitivity of the proton transfer with respect to the choice of different basis sets and density functional (PBE-D3-DZVP and BLYP-D3-DZVP), a cubic box containing 64 water molecules with a length of 12.48 \AA (corresponding to 1.0 g/cm³ density) was also constructed. The validation tests are presented in Sec. S4 in the Supplementary Information (SI). The protocol of these reference simulations in the bulk solution was similar to the clusters, with the only difference being that the system used PBC. All AIMD simulations were performed in the canonical

ensemble at 300 K with a Nosé–Hoover thermostat (3 chains) at the time constant of 100 fs to regulate the temperature.

The choice of this solver is discussed in Sec. S5 in SI.

S4. Protocol validation for AIMD parameters by testing them in bulk solution simulations

The radial distribution function (RDF) between atoms of water molecules was analyzed to verify the accuracy of our simulation parameters settings and results. The data for our simulated control group was mainly selected from previous work done by Kuo et al.^{S31} The data for the experimental control group was chosen from the work of Soper,^{S34} Chen et al.^{S32} and Cheng et al.,^{S33} respectively. All the details of the simulations and experiments in the control group are labelled in Fig. S1 and Fig. S2 and summarized in Table S1 for a more precise presentation. For the RDF between the oxygen atoms of the water molecules, it can be found that the simulation and experimental results agree at the first neighborhood of the water molecules, at 2.75 Å. However, there are some discrepancies in the peaks, which range from 2.85 to 3.21, with the mean of the data at 3.01 ± 0.13 . The relevant data are included in Table S2. The results of our two simulations with different combinations are similar. We also calculated the coordination number (CN) for the water molecules first and second nearest neighbours. The CNs were determined by calculating the oxygen-oxygen number integral at the location of the first minimum in the associated RDF. We can find that in the first shell, the CNs of the water molecules are very near to 4. All the simulation algorithms from Kuo et al.’s and other experimental results show a high degree of agreement in the first peak of the RDFs, with Monte Carlo calculations using CP2K^{S18} in the NVT ensemble at 315 K, simulation using Car-Parrinello Molecular Dynamics (CPMD) code^{S35} in the NVT ensemble at 315 K (with the value of the fictitious electron mass at $\mu = 400$ a.u.), and simulation using CPMD in the NVE ensemble at 313 K. Moreover, there is good correspondence with our work at the second peak. However, one of the simulations using CPMD^{S35} at 315 K in

the NVT ensemble (with the more significant value of the fictitious electron mass at $\mu = 800$ a.u.) and one using CP2K^{S18} in the NVE ensemble at 328 K, and the experimental results of Soper’s show some minor deviations from our results in the second peak. Yet Kuo et al. argued using a $\mu = 800$ a.u value ensures stable CPMD trajectories for simulations in the canonical ensemble while employing large thermostats of the nuclear and electronic degrees of freedom.

Table S1: Details of the setup of the simulations used to compare them with each other in Fig. S1 and Fig. S2. MC denotes Monte Carlo simulations. The designations ‘i’ and ‘ie’ represent the use of massive thermostats specifically for the ionic degrees of freedom or both ionic and electronic degrees of freedom, respectively. Some simulations used two distinct options for the fictitious electron mass: a small value of $\mu = 400$ a.u. and a larger value of $\mu = 800$ a.u. Δt and t_{prod} are the timestep and length of production run.^{S31}

	functional	basis set	pseudopotential	cut-off [Ry]	μ [a.u.]	N	Δt [fs]	t_{prod} [ps]	T [K]
CP2K-MD-NVT	PBE-D3	DZVP	GTH	400	n/a	64	0.5	5	300
CP2K-MD-NVT	BLYP-D3	DZVP	GTH	400	n/a	64	0.5	5	300
CP2K-MC-NVT	BLYP	TZV2P	GTH	280	n/a	64	n/a	n/a	315
CPMD-NVT-i400	BLYP	PW	TM	85	400	64	0.097	11.1	315
CPMD-NVT-ie800	BLYP	PW	TM	85	800	64	0.097	7.2	315
CP2K-MD-NVE	BLYP	TZV2P	GTH	280	n/a	64	0.5	12.0	328
CPMD-NVE-400	BLYP	PW	TM	85	n/a	64	0.48	11.4	328
PIMD-NVT	PBE-rVV10	PW	norm-conserving	85	n/a	32	0.5	8.0	300
PIMD-NVT	revPBE0-D3	TZV2P	GTH	400	n/a	64	0.5	100	300

Table S2: Comparison of g_{OO} simulation and experiment results in Fig. S1(a). The values of the height and location of the first peak in the oxygen-oxygen RDFs, as well as the oxygen-oxygen CNs are presented.

	functional	basis set	pseudopotential	$r_{OO,max}$ [Å]	$g_{OO,max}$	CN
CP2K-MD-NVT	PBE	DZVP	GTH	2.75	3.14	3.96
CP2K-MD-NVT	BLYP-D3	DZVP	GTH	2.75	3.21	4.01
CP2K-MC-NVT	BLYP	TZV2P	GTH	2.75	3.0	4.0
CPMD-NVT-i400	BLYP	PW	TM	2.75	3.0	4.0
CPMD-NVT-ie800	BLYP	PW	TM	2.75	2.9	4.0
CP2K-MD-NVE	BLYP	TZV2P	GTH	2.75	3.1	4.0
CPMD-NVE-400	BLYP	PW	TM	2.75	2.9	4.0
Experiment	n/a	n/a	n/a	2.75	2.85	4.0

The RDFs of oxygen-hydrogen and hydrogen-hydrogen atom pairs were also calculated. Our results for the RDFs between hydrogen and oxygen atoms perfectly agree with the

experimental results at the first peak. They differ somewhat from the other simulations, but all the results generally have a similar trend. Our simulation results vary slightly from all other experiments and simulations for the RDFs between hydrogen and hydrogen atoms but still follow the same trend. These results are shown in Fig. S2. By calculating the RDFs between different atoms of water molecules in the 64-water bulk system and comparing them with other typical simulation and experimental results, we can see that our results are accurate and the simulation parameters are set up correctly. The simulation results are similar by combining two different basis sets and density functional approximations, PBE-D3-DZVP and BLYP-D3-DZVP.

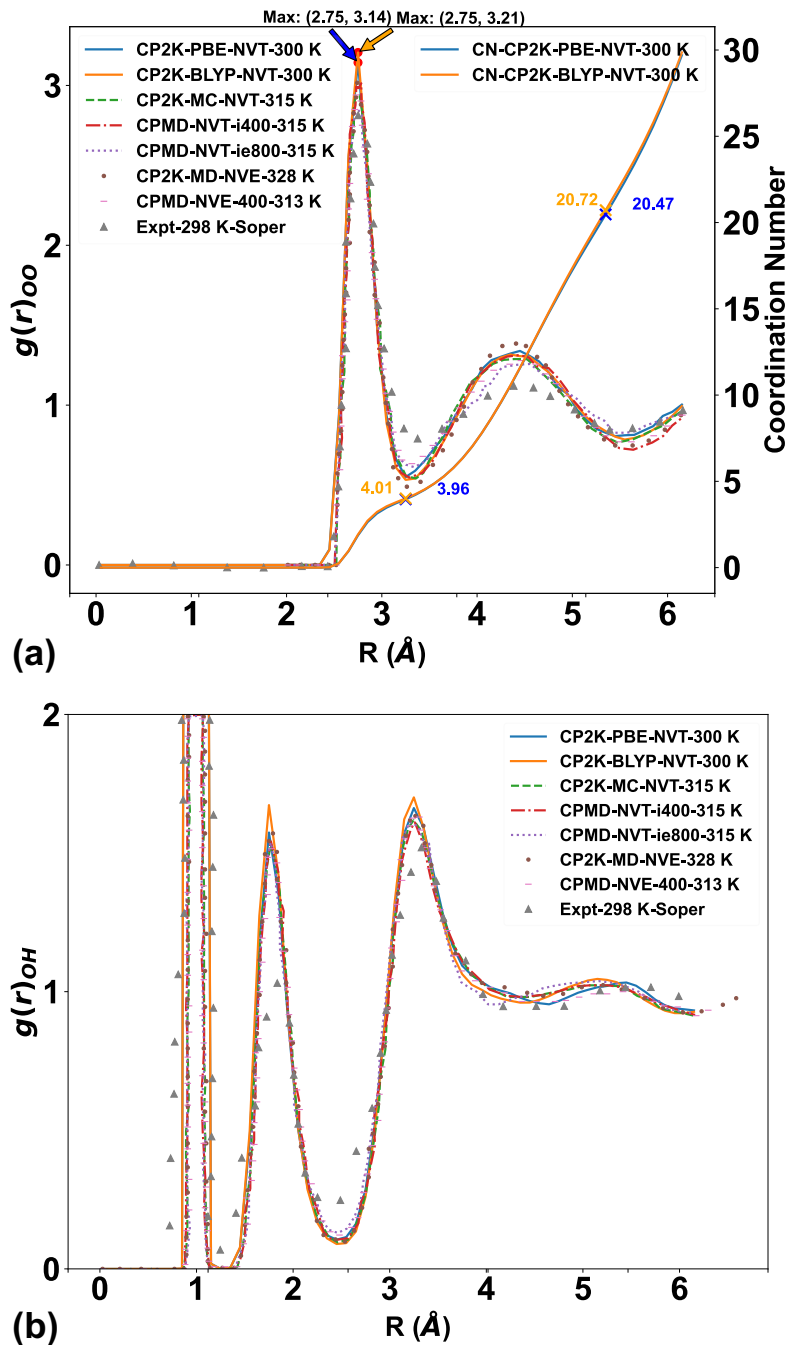


Figure S1: Comparison of g_{OO} (a) and g_{OH} (b) derived from simulations and experiment results. The cases ‘CP2K-PBE-D3-DZVP’ and ‘CP2K-BLYP-D3-DZVP’ correspond to the results of our simulations of 64 H₂O bulk at 300 K. The cases ‘CP2K-MC-NVT’, ‘CPMD-NVT-i400’, and ‘CPMD-NVT-ie800’ are the different AIMD simulations at 315 K by Kuo et al.^{S31} The cases ‘CP2K-MD-NVE-328 K’ and ‘CPMD-NVE-400-313 k’ are also AIMD simulations in NVE ensemble by Kuo et al.^{S31} The cases ‘PIMD-NVT-300 K’ and ‘ML-Potential-PIMD-NVT-300 K’ are the path-integral MD simulation by Chen et al.^{S32} and Cheng et al.,^{S33} respectively. The cases ‘Expt-298 K’ correspond the experimental investigations by Chen et al.^{S32} and Soper.^{S34} The coordination number of water molecules for the g_{OO} results is shown in (a).

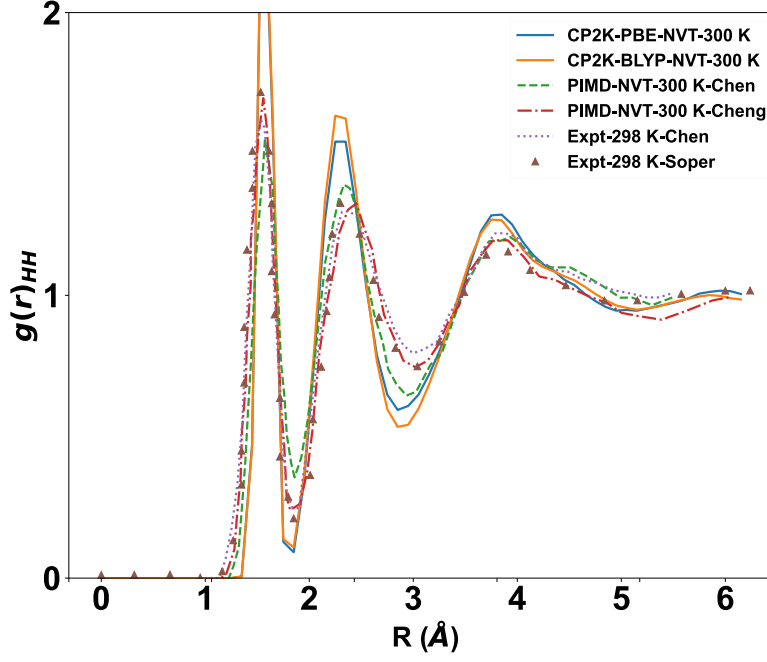


Figure S2: Comparison of g_{HH} derived from simulations and experiment results. The cases ‘CP2K-PBE-D3-DZVP’ and ‘CP2K-BLYP-D3-DZVP’ correspond to the results of our simulations of 64 H₂O bulk at 300 K. The cases ‘CP2K-MC-NVT’, ‘CPMD-NVT-i400’, and ‘CPMD-NVT-ie800’ are the different AIMD simulations at 315 K by Kuo et al.^{S31} The cases ‘CP2K-MD-NVE-328 K’ and ‘CPMD-NVE-400-313 k’ are also AIMD simulations in *NVE* ensemble by Kuo et al..^{S31} The cases ‘PIMD-NVT-300 K’ and ‘ML-Potential-PIMD-NVT-300 K’ are the path-integral MD simulation by Chen et al.^{S32} and Cheng et al.,^{S33} respectively. The cases ‘Expt-298 K’ correspond the experimental investigations by Chen et al.^{S32} and Soper.^{S34}

S5. Selection of the Poisson solver

The choice of Poisson solver can significantly impact the accuracy and reliability of the results when computational simulations involving isolated systems. Different solvers were designed to solve the Poisson equation,

$$\nabla^2\phi(\mathbf{r}) = -\frac{\rho(\mathbf{r})}{\epsilon_0} \tag{1}$$

where ∇^2 is the Laplacian operator, $\phi(\mathbf{r})$ is the electrostatic potential, $\rho(\mathbf{r})$ is the charge density at position \mathbf{r} , ϵ_0 is the permittivity of free space. The Poisson solvers handle the electrostatic potential and boundary conditions in distinct ways, which can lead to variations in the computed properties of the system. To understand these differences, comparing and discussing the simulation results produced by different Poisson solvers is essential. In this work, we focus on two specific Poisson solvers: the WAVELET^{S29,S30} and the MT (Martyna-Tuckerman).^{S36}

One of the significant advantages of the wavelet-based Poisson solver is its flexibility in handling boundary conditions. Unlike traditional methods that may require artificial periodicity or complex boundary condition treatments, wavelets naturally accommodate a variety of boundary conditions, including Dirichlet,^{S37} Neumann,^{S37} or mixed boundary conditions. This makes the method well-suited for isolated systems or systems with complex geometries. Hence, we prefer the WAVELET solver for calculating our neutral and charged clusters. The MT^{S36} Poisson solver is another advanced method implemented in CP2K to address the issues of simulating systems with partial periodicity within a computational framework that generally uses PBC. It is useful for simulations where we need to minimize or eliminate the artificial interactions between periodic images, making it ideal for systems like slabs, surfaces, or even clusters that are non-periodic in at least one dimension.

Analyzing the simulation results using these two approaches, we can gain insight into their respective strengths and limitations and their suitability for different isolated systems.

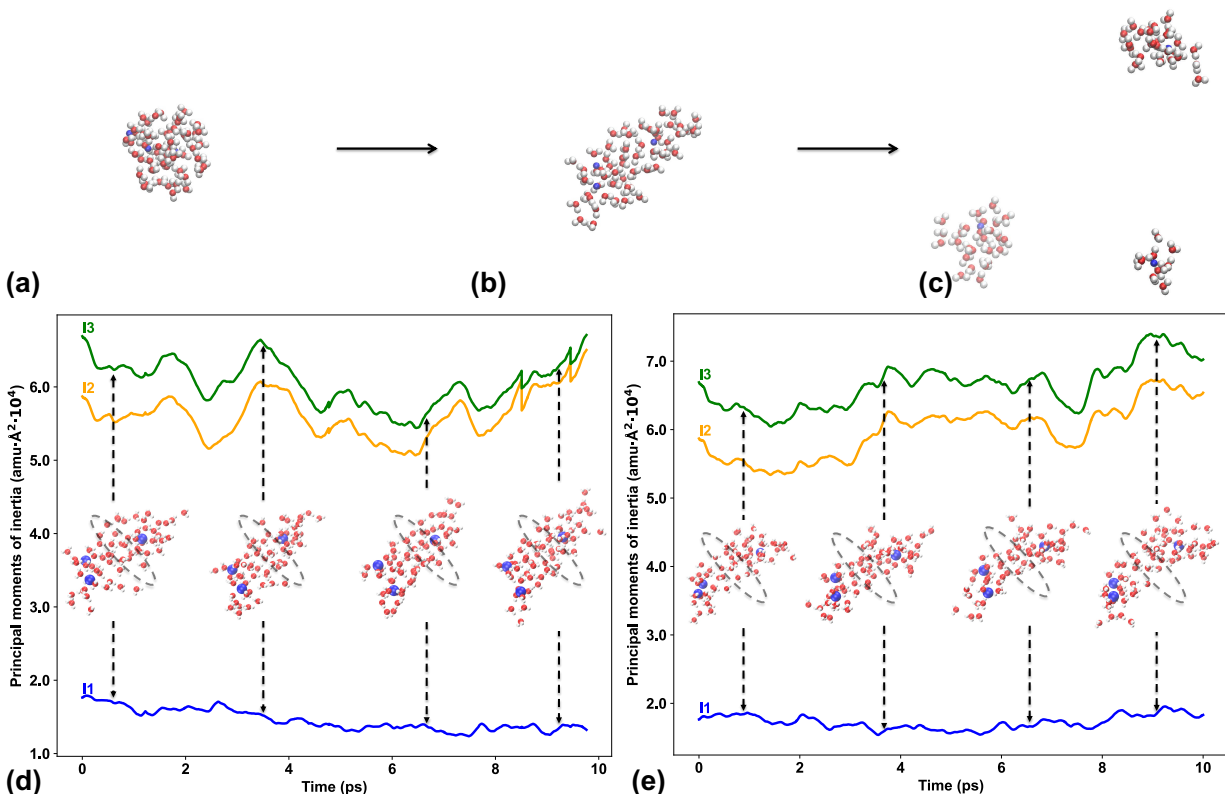


Figure S3: (a) The initial configuration of the 64-water cluster containing three Na⁺. (b) A typical intermediate configuration of the 64-H₂O-3Na⁺ cluster before separating into three sub-clusters. This configuration was used as the initial configuration for performing AIMD simulation in CP2K. (c) The final configuration of the 64-H₂O-3Na⁺ cluster separates into three sub-clusters after 1 ns MD simulation in the *NVT* ensemble. Configuration (b) is used to initiate a CP2K run up to 10 ps using the WAVELET Poisson solver for which the configuration after 10 ps is shown in (d) and using the MT Poisson solver shown in (e). The principal moments of inertia reflect the extension and contraction of the cluster in different directions, respectively. As the simulation progresses, the elliptical dashed line in (d) and (e) marks snapshots of the simulation that show a progressively narrower bottleneck in the junction, reflecting a tendency for the entire cluster to divide into two sub-clusters.

This comparison will help elucidate how the choice of Poisson solver influences the physical observables of interest and contribute to a more informed selection of computational methods in further studies. Before we finally chose which Poisson solver to use in the 64-water cluster containing three hydroniums, we prepared a 64-water cluster containing three Na^+ ions and counter ions in the $80 \times 80 \times 80$ cubic cell to make a similar system, as shown in Fig. S3 a. We performed MD simulations up to 1 ns for this system in the NVT ensemble using the LAMMPS (21 Nov 2023 version) package.^{S38} We used the Multi-Level Summation Method (MSM) solver^{S17} to compute long-range interactions in MD simulations with non-PBC. The entire cluster was placed in the centre of a cubic vacuum box with dimensions $50 \times 50 \times 50 \text{ \AA}^3$. Then the counterions were placed close to the edge of the cubic box to ensure that the interaction force of the counterions on the clusters was negligible. The final configuration of the MD simulation, as shown in Fig. S3 (c), presents the division of the whole cluster into three sub-clusters, each containing a solvated Na^+ ion. Fig. S3 (b) shows the configuration before the cluster separates, which tends to separate as shown by its elongation but is still connected. We then used the configuration from Fig. S3 (b) as our initial structure in CP2K and continued with the AIMD simulation. We applied WAVELET and MT Poisson solvers in this simulation to handle the electrostatic forces in a non-PBC setting. After 10 ps throughout the simulation, we observe a tendency for one of the Na^+ ions to separate from the cluster in both simulations, as shown in the snapshots of the simulations in Figs. S3 (d) and Fig. S3 (e), respectively. The whole cluster continues to elongate as the simulation proceeds, and the grey dashed circles mark that the cluster becomes gradually narrower in the interior, with a tendency to divide. This conformational elongation and deformation process is also clearly monitored by the principal moments of inertia parameter. The main axis I1 in Fig. S3 (d) and Fig. S3 (e) are through the cluster and orientated parallel to its elongation direction.

Comparing these two figures, we can see that the simulation results using WAVELET in Fig. S3 (d) more logically illustrate that the principal moments of inertia for this axis I1

show a decreasing trend, corresponding to the other two parameters of the axis I2 and I3 that go through the cluster but are oriented perpendicularly to the axis I1 show an increasing trend. This reflects a process whereby the cluster is elongated, and more molecules fit more closely to the I1 axis and are distributed along the elongated direction. Hence, we will use this WAVELET Poisson solver to handle the charged clusters in our main work.

S6. Radial distribution functions between oxygen and Fe^{3+} , Lu^{3+} , and La^{3+} in aqueous clusters

Table S3: Location of the maxima and coordination number (CN) of the RDF between a trivalent ion and oxygen sites of TIP3P water in $N_{\text{H}_2\text{O}} = 78$ at 190 K. The location of the maxima in the RDF peaks in each solvation shell is in Å. $\text{CN}^{(n)}$ ($n = 1 - 4$) denotes the coordination number in each solvation shell.

Ion	1st max	$\text{CN}^{(1)}$	2nd max	$\text{CN}^{(2)}$	3rd max	$\text{CN}^{(3)}$	4th max	$\text{CN}^{(4)}$
Fe^{3+}	1.6	3.5	2.9	7	4.1	16	5.3	53
Lu^{3+}	2.3	7	3.5	9	4.5	23	6.3	52
La^{3+}	2.6	9	4.9	28	6.6	54		

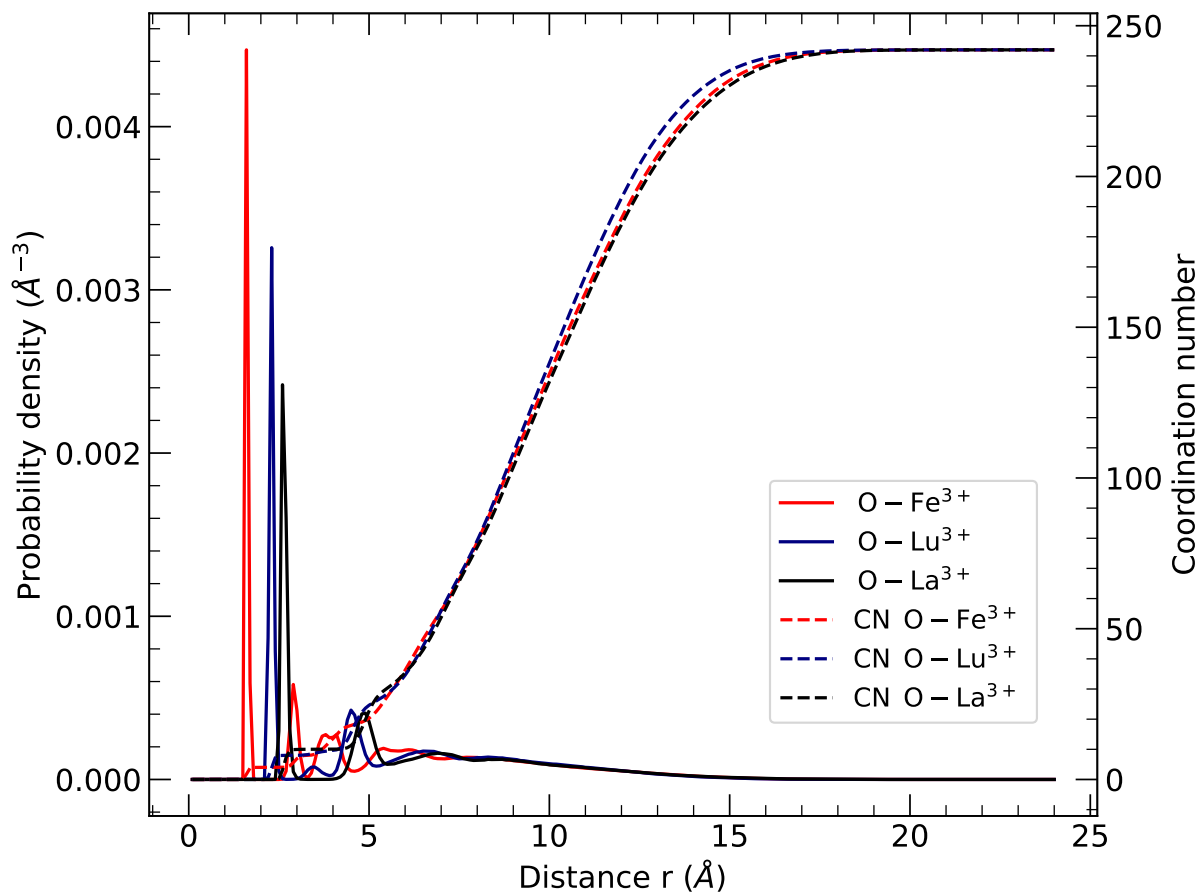


Figure S4: Radial distribution function (RDF) and coordination number between oxygen sites of H₂O and Fe³⁺ ion (red colored line), Lu³⁺-O (blue colored line), and La³⁺-O (black colored line) in $N_{\text{H}_2\text{O}} = 242$ at $T = 190$ K.

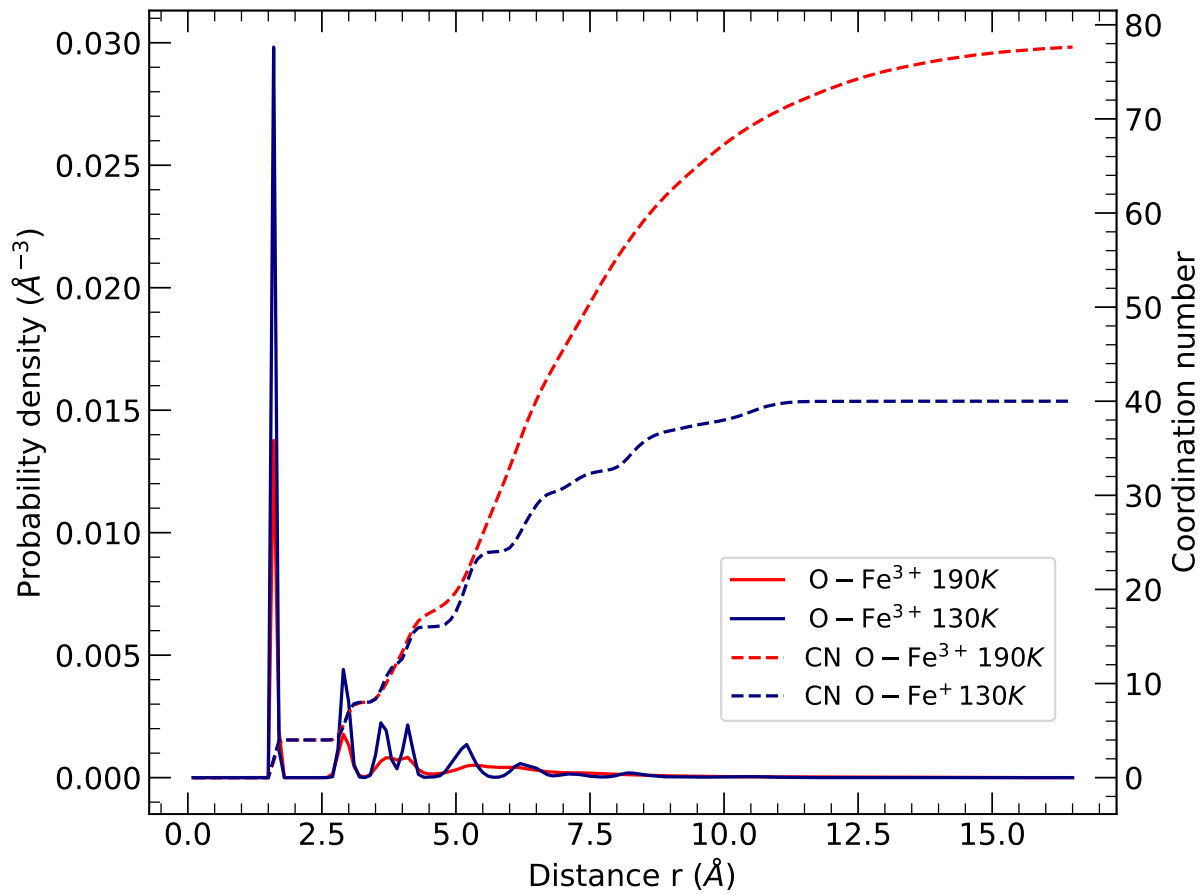
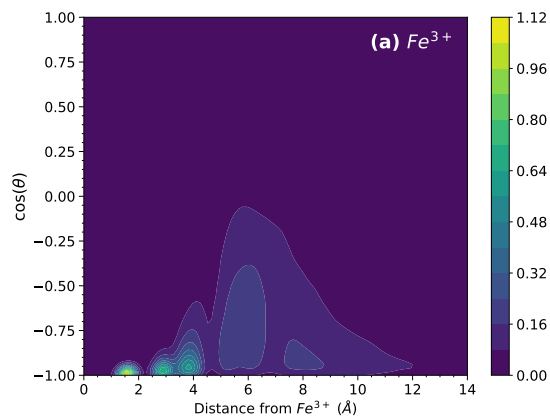
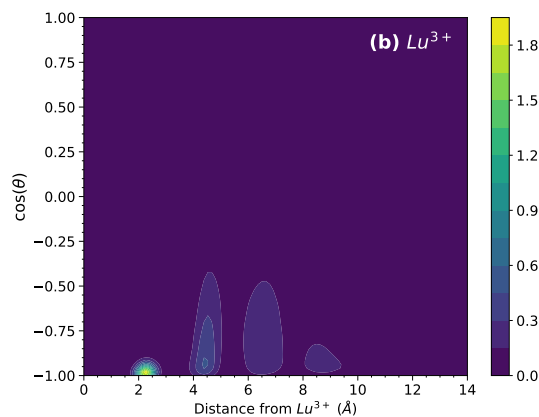


Figure S5: RDF and coordination number for O-Fe³⁺ when $N_{\text{H}_2\text{O}} = 40$ at $T = 130$ K compared with O-Fe³⁺ when $N_{\text{H}_2\text{O}} = 78$ at $T = 190$ K.

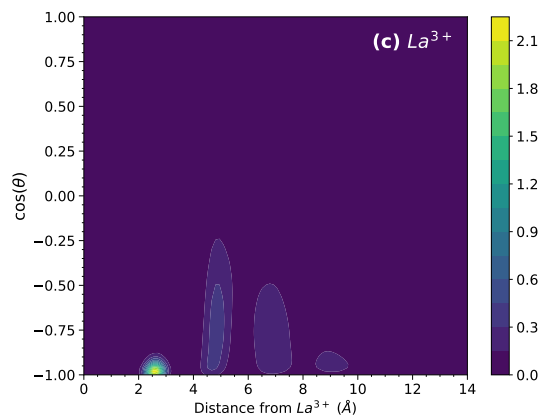
S7. Distribution of $\cos(\theta)$ around Fe^{3+} , Lu^{3+} , or La^{3+} in aqueous clusters



(a)



(b)



(c)

Figure S6: Contour maps of $\cos(\theta)$ distribution of H_2O dipole orientations within successive spherical shells centered at (a) Fe^{3+} , (b) Lu^{3+} , and (c) La^{3+} in $N_{\text{H}_2\text{O}} = 78$ at 190 K.

S8. Ring structures in clusters comprising 64 H_2O -3 H_3O^+ ions studied by AIMD

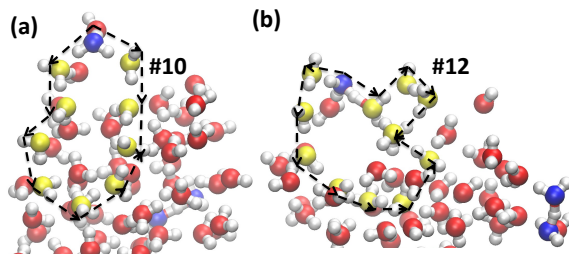


Figure S7: Snapshots of the two longer ring structures composing of (a) 10 and (b) 12 H_2O molecules from the AIMD trajectory of the 64 H_2O - 3 H_3O^+ cluster. These rings appear with low probability in the 7 ps AIMD run. The color coding of the atomic sites is the same as that in Fig. 8 in the main text. Here, the oxygen sites in the rings are highlighted in yellow. The paths for proton transfer along the rings are indicated by using the dashed arrows.

References

- (S1) Phillips, J. C.; Hardy, D. J.; Maia, J. D. C.; Stone, J. E.; Ribeiro, J. V.; Bernardi, R. C.; Buch, R.; Fiorin, G.; Hénin, J.; Jiang, W.; McGreevy, R.; Melo, M. C. R.; Radak, B. K.; Skeel, R. D.; Singharoy, A.; Wang, Y.; Roux, B.; Aksimentiev, A.; Luthey-Schulten, Z.; Kalé, L. V.; Schulten, K.; Chipot, C.; Tajkhorshid, E. Scalable molecular dynamics on CPU and GPU architectures with NAMD. *J. Chem. Phys.* **2020**, *153*, 044130.
- (S2) Humphrey, W.; Dalke, A.; Schulten, K. VMD – Visual Molecular Dynamics. *J. Mol. Graph.* **1996**, *14*, 33–38.
- (S3) MacKerell Jr, A. D.; Bashford, D.; Bellott, M.; Dunbrack Jr, R. L.; Evanseck, J. D.; Field, M. J.; Fischer, S.; Gao, J.; Guo, H.; Ha, S., et al. All-atom empirical potential for molecular modeling and dynamics studies of proteins. *J. Phys. Chem. B* **1998**, *102*, 3586–3616.
- (S4) Won, Y. Force field for monovalent, divalent, and trivalent cations developed under the solvent boundary potential. *J. Phys. Chem. A* **2012**, *116*, 11763–11767.
- (S5) Guàrdia, E.; Padró, J. Molecular dynamics simulation of ferrous and ferric ions in water. *Chemical physics* **1990**, *144*, 353–362.
- (S6) Kneifel, C.; Newton, M.; Friedman, H. Simulation of solvent isotope effects on aqueous ferrous and ferric ions. *Journal of Molecular Liquids* **1994**, *60*, 107–145.
- (S7) Amira, S.; Spångberg, D.; Probst, M.; Hermansson, K. Molecular dynamics simulation of Fe²⁺ (aq) and Fe³⁺ (aq). *J. Phys. Chem. B* **2004**, *108*, 496–502.
- (S8) Li, P.; Song, L. F.; Merz Jr, K. M. Parameterization of highly charged metal ions using the 12-6-4 LJ-type nonbonded model in explicit water. *J. Phys. Chem. B* **2015**, *119*, 883–895.

- (S9) Fiorin, G.; Klein, M. L.; Hénin, J. Using collective variables to drive molecular dynamics simulations. *Mol. Phys.* **2013**, *111*, 3345–3362.
- (S10) Hardy, D. J.; Stone, J. E.; Schulten, K. Multilevel summation of electrostatic potentials using graphics processing units. *Parallel Comput.* **2009**, *35*, 164–177.
- (S11) Swope, W. C.; Andersen, H. C.; Berens, P. H.; Wilson, K. R. A computer simulation method for the calculation of equilibrium constants for the formation of physical clusters of molecules: Application to small water clusters. *J. Chem. Phys.* **1982**, *76*, 637–649.
- (S12) Martínez, L.; Andrade, R.; Birgin, E. G.; Martínez, J. M. PACKMOL: A package for building initial configurations for molecular dynamics simulations. *J. Comp. Chem.* **2009**, *30*, 2157–2164.
- (S13) Plimpton, S. Fast parallel algorithms for short-range molecular dynamics. *J. Comp. Phys.* **1995**, *117*, 1–19.
- (S14) Wu, Y.; Tepper, H. L.; Voth, G. A. Flexible simple point-charge water model with improved liquid-state properties. *J. Chem. Phys.* **2006**, *124*, 024503.
- (S15) Vácha, R.; Buch, V.; Milet, A.; Devlin, J. P.; Jungwirth, P. Autoionization at the surface of neat water: is the top layer pH neutral, basic, or acidic? *Phys. Chem. Chem. Phys.* **2007**, *9*, 4736–4747.
- (S16) Bonthuis, D. J.; Mamatkulov, S. I.; Netz, R. R. Optimization of classical nonpolarizable force fields for OH^- and H_3O^+ . *J. Chem. Phys.* **2016**, *144*, 104503.
- (S17) Hardy, D. J. *Multilevel summation for the fast evaluation of forces for the simulation of biomolecules*; University of Illinois at Urbana-Champaign, 2006.
- (S18) Kühne, T. D.; Iannuzzi, M.; Del Ben, M.; Rybkin, V. V.; Seewald, P.; Stein, F.; Laino, T.; Khaliullin, R. Z.; Schütt, O.; Schiffmann, F., et al. CP2K: An electronic

- structure and molecular dynamics software package-Quickstep: Efficient and accurate electronic structure calculations. *J. Chem. Phys.* **2020**, *152*, 194103.
- (S19) VandeVondele, J.; Hutter, J. An efficient orbital transformation method for electronic structure calculations. *J. Chem. Phys.* **2003**, *118*, 4365–4369.
- (S20) Lippert, G.; Hutter, J.; Parrinello, M. The Gaussian and augmented-plane-wave density functional method for ab initio molecular dynamics simulations. *Theor. Chem. Acc.* **1999**, *103*, 124–140.
- (S21) VandeVondele, J.; Hutter, J. Gaussian basis sets for accurate calculations on molecular systems in gas and condensed phases. *J. Chem. Phys.* **2007**, *127*, 114105.
- (S22) Perdew, J. P.; Burke, K.; Ernzerhof, M. Generalized gradient approximation made simple. *Phys. Rev. Lett.* **1996**, *77*, 3865.
- (S23) Becke, A. D. Density-functional exchange-energy approximation with correct asymptotic behavior. *Phys. Rev. A* **1988**, *38*, 3098.
- (S24) Lee, C.; Yang, W.; Parr, R. G. Development of the Colle-Salvetti correlation-energy formula into a functional of the electron density. *Phys. Rev. B* **1988**, *37*, 785.
- (S25) Grimme, S. Semiempirical GGA-type density functional constructed with a long-range dispersion correction. *J. Comp. Chem.* **2006**, *27*, 1787–1799.
- (S26) Knight, C.; Lindberg, G. E.; Voth, G. A. Multiscale reactive molecular dynamics. *J. Chem. Phys.* **2012**, *137*, 22A525.
- (S27) Goedecker, S.; Teter, M.; Hutter, J. Separable dual-space Gaussian pseudopotentials. *Phys. Rev. B* **1996**, *54*, 1703.
- (S28) Marx, D.; Hutter, J. *Ab initio molecular dynamics: basic theory and advanced methods*; Cambridge University Press, 2009.

- (S29) Genovese, L.; Deutsch, T.; Neelov, A.; Goedecker, S.; Beylkin, G. Efficient solution of Poisson’s equation with free boundary conditions. *J. Chem. Phys.* **2006**, *125*, 074105.
- (S30) Genovese, L.; Deutsch, T.; Goedecker, S. Efficient and accurate three-dimensional Poisson solver for surface problems. *J. Chem. Phys.* **2007**, *127*, 054704.
- (S31) Kuo, I.-F. W.; Mundy, C. J.; McGrath, M. J.; Siepmann, J. I.; VandeVondele, J.; Sprik, M.; Hutter, J.; Chen, B.; Klein, M. L.; Mohamed, F., et al. Liquid water from first principles: Investigation of different sampling approaches. *J. Phys. Chem. B* **2004**, *108*, 12990–12998.
- (S32) Chen, W.; Ambrosio, F.; Miceli, G.; Pasquarello, A. Ab initio electronic structure of liquid water. *Phys. Rev. Lett.* **2016**, *117*, 186401.
- (S33) Cheng, B.; Engel, E. A.; Behler, J.; Dellago, C.; Ceriotti, M. Ab initio thermodynamics of liquid and solid water. *Proc. Natl. Acad. Sci. U.S.A.* **2019**, *116*, 1110–1115.
- (S34) Soper, A. K. The radial distribution functions of water as derived from radiation total scattering experiments: Is there anything we can say for sure? *Int. Sch. Res. Notices.* **2013**, *2013*, 279463.
- (S35) Hutter, J.; Iannuzzi, M. CPMD: Car-Parrinello molecular dynamics. *Z. Kristallogr. Cryst. Mater.* **2005**, *220*, 549–551.
- (S36) Martyna, G. J.; Tuckerman, M. E. A reciprocal space based method for treating long range interactions in ab initio and force-field-based calculations in clusters. *J. Chem. Phys.* **1999**, *110*, 2810–2821.
- (S37) Evans, L. C. *Partial differential equations*; American Mathematical Society, 2022; Vol. 19.
- (S38) Thompson, A. P.; Aktulga, H. M.; Berger, R.; Bolintineanu, D. S.; Brown, W. M.; Crozier, P. S.; In’t Veld, P. J.; Kohlmeyer, A.; Moore, S. G.; Nguyen, T. D., et al.

LAMMPS-a flexible simulation tool for particle-based materials modeling at the atomic, meso, and continuum scales. *Comput. Phys. Commun.* **2022**, *271*, 108171.